

We are IntechOpen, the world's leading publisher of Open Access books Built by scientists, for scientists

6,300

Open access books available

171,000

International authors and editors

190M

Downloads

Our authors are among the

154

Countries delivered to

TOP 1%

most cited scientists

12.2%

Contributors from top 500 universities



WEB OF SCIENCE™

Selection of our books indexed in the Book Citation Index
in Web of Science™ Core Collection (BKCI)

Interested in publishing with us?
Contact book.department@intechopen.com

Numbers displayed above are based on latest data collected.
For more information visit www.intechopen.com



Numerical Analysis of the Liquid-Gas-Solid Three Phase Flow Inside AWJ Nozzle

Xinping Long and Qi Liu

Additional information is available at the end of the chapter

<http://dx.doi.org/10.5772/intechopen.75938>

Abstract

The multiphase flows inside the two abrasive waterjet (AWJ) nozzles with different abrasive inlet tube angles are simulated using the standard $k-\varepsilon$ turbulence model based on the Euler-Lagrangian approach. The volume of fluid (VOF) method is employed to simulate the water-air multiphase flows. And, the abrasive particles are treated as dilute dispersed phase and tracked with the discrete particle method (DPM). The results indicate that the abrasive inlet tube angle has little impact on the water-phase flows. Further analysis shows that a larger abrasive inlet tube angle can enhance the particle accelerations. The particle number independence analysis is conducted, and the results indicate that sufficient particles should be tracked in order to obtain statistically representative results. The effects of particle initial velocities, particle shape factors, and the restitution coefficients on the predicted particle movements are further analyzed for the two nozzles with abrasive inlet tube angles of 45° and 60° . The results reveal that at the current velocity range, the particle initial velocities have little impact on the predicted particle velocities. However, both the shape factors and the restitution coefficients play an important role on the calculated particle velocities. The results provide a deeper understanding of particle acceleration performance inside the AWJ nozzles with different abrasive inlet tube angles.

Keywords: abrasive waterjet, multiphase flow, DPM, VOF

1. Introduction

The abrasive waterjet (AWJ) is originally developed to improve the cutting ability of the pure waterjet (PWJ). As a new type of cold cutting technology, the AWJ is performed to cut target materials with water-containing abrasive particles at high pressures. Generally, the AWJ is capable of cutting or manufacturing both brittle and ductile materials without imposing thermal

impact on the target materials. It also has the advantages of high machining versatility, small machining force, and high flexibility compared with other manufacturing methods. Therefore, the AWJ has been widely applied in numerous fields [1–4]. Recently, the potential of the AWJ technology for high precision cutting or manufacturing of hard-to-machine materials has made the AWJ again receive much attention [5, 6].

It should be mentioned that the AWJ is different from the abrasive slurry jet (ASJ). And, the definition of the two types is mainly based on the mixing process of abrasive particles with fluid. For the ASJ, in the high-pressure tank, the abrasive particles are premixed with water to produce the so-called slurry which is directly ejected from the nozzle. However, for the AWJ, as illustrated in **Figure 1**, the high-pressure pure water is firstly ejected from the orifice into the mixing chamber where the abrasive particles and the air are simultaneously entrained to mix with the high-speed water, and then the AWJ is generated in the focus tube. Therefore, there are only two phases of flows (particle and water) in ASJ nozzle but three phases of flows (particle, water, and air) in AWJ nozzle. The operating pressure of AWJ is much higher than that of the ASJ, and the energy utilization of AWJ is comparatively lower. Thus, extensive efforts have already been made to investigate the cutting, machining, and energy transfer efficiency of the so-called AWJ technology [7, 8]. Momber investigated the energy transfer during the high-speed waterjet formation process and also the abrasive particle mixing and

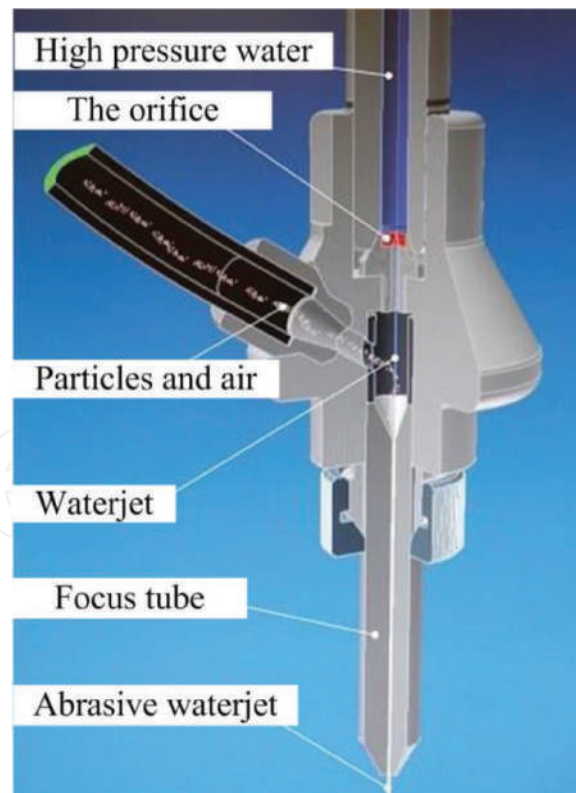


Figure 1. The AWJ cutting system and AWJ nozzle [6].

acceleration processes by conducting impact-force measurements [7]. Lee et al. studied the material removal mechanisms of AWJ with micro-sized abrasive particles [9]. Shanmugam and Masood experimentally investigated the effects of AWJ operating parameters on the kerf taper angle of two types of layered composites [10]. Coray et al. tested a 5:1 scale AWJ equipment models to study the kinetic energy distributions of the abrasive particles together with the jet structure. They reported that due to the strong interactions among the three phases the signal differences between water phase and abrasive particles could not yet be distinguished experimentally [11].

It is already well known that the AWJ nozzle, as an important component of the AWJ equipment, has a significant impact on the overall manufacturing performances and is crucial for improving machining quality and reducing energy consumption. Thus, a better understanding of the effects of nozzle parameters on the jet structure and abrasive particle movements is essential to develop high-performance AWJ equipment. However, due to the small dimensions of the AWJ nozzle and the highly aggressiveness of abrasive particles, conducting experiments to study the three phases of flows inside the AWJ nozzle is still very challenging. And, the accurate measurement of the complex multiphase flows which involves ultrahigh-speed water, air, and abrasive particles inside the extremely small nozzle space may even impossible at present. With the rapid development of computational fluid dynamics (CFD) and computing ability, numerical simulations of this complex internal flows have been made possible, which provides an effective way to gain a better understanding of the multiphase interaction mechanisms. Long et al. conducted numerical simulations to investigate the particle movement inside the AWJ nozzle using different particle shape factors. The results revealed that a smaller particle shape factor could enhance the overall particle acceleration process [6]. Yang et al. numerically studied the abrasive particle motions and the corresponding erosion rate inside the AWJ nozzle at the pressures beyond 300 MPa. It was revealed that the proposed numerical model provided a reliable way to investigate the AWJ nozzle internal multiphase flows [12]. Basha et al. simulated the internal multiphase flows inside an AWJ nozzle and investigated the jet flow dynamic characteristics. It was confirmed that the numerical simulations could accurately capture the AWJ nozzle performance [13].

Despite the abovementioned efforts, the complex interactions between the fluid phases and the particles inside the AWJ nozzle are not yet fully understood, and the effects of numerical model parameters on the simulation results are not well investigated. Also, the effects of nozzle structure on the multiphase flows are not well studied. Inspired by the mentioned work, the present paper is devoted to investigating the liquid-gas-solid multiphase flows in AWJ nozzles with different abrasive inlet tube angles at a given high operating pressure under different model parameters based on three-dimensional Euler-Lagrangian numerical simulations. The effects of particle initial velocities, particle shape factors, and particle-wall restitution coefficients on the predicted particle velocities are discussed. The effects of abrasive inlet tube angles on the multiphase flows are further analyzed. The results can help to provide guidance for future CFD-aided AWJ nozzle optimization.

2. Governing equations and numerical method

As illustrated in **Figure 1**, the high-pressure water is firstly ejected from the orifice, and the resulted high-speed water jet then enters into the mixing chamber. By the high-speed jet entraining effects, the air phase together with the abrasive particles is entrained into the mixing chamber where strong interactions are expected. The abrasive particles are mixed and accelerated by the high-speed fluid phase and finally ejected through the long focus tube to impact on the workpiece. The present study is performed by simulating the steady-state multiphase flows in AWJ nozzles based on the time-averaged Navier-Stokes equations. It was reported that the volume fractions of the abrasive particles in the AWJ nozzle was normally less than 10% [14]. Thus, the Euler-Lagrangian method is finally utilized for all the present simulations. Both the water phase and the air phase are treated as continuums and are computed in Eulerian reference frame using the finite volume method. However, the abrasive particles are considered as discrete phase and are solved in Lagrangian reference frame using the discrete particle method (DPM).

2.1. Governing equations for continuous phases

The water-air multiphase flows are modeled using the volume of fluid (VOF) model. The volume fraction-based composition of AWJ is approximately 0.2–0.5% abrasive particles, 4–6% water phase, and 93–95% air phase [15]. The air phase is finally chosen as the primary phase in the present simulations, and thus the continuity equation for the volume fraction of the water phase can be written as

$$\frac{\partial(\alpha_w u_i)}{\partial x_i} = 0 \quad (1)$$

where α_w is the volume fraction of water and u_i is velocity. The volume fraction of the primary phase α_a can be directly obtained by the simple equation:

$$\alpha_a = 1.0 - \alpha_w \quad (2)$$

As the VOF is based upon the single fluid assumption, the air phase and the water phase share the same velocity field, and a single momentum equation is solved throughout the computational domain. Therefore, the governing equation for the conservation of momentum can be given as

$$\frac{\partial(\rho u_i u_j)}{\partial x_j} = -\frac{\partial p}{\partial x_i} + \frac{\partial}{\partial x_j} \left[(\mu + \mu_t) \left(\frac{\partial u_i}{\partial x_j} + \frac{\partial u_j}{\partial x_i} - \frac{2}{3} \frac{\partial u_k}{\partial x_k} \delta_{ij} \right) \right] \quad (3)$$

where u_i and u_j are the velocities in the x_i and x_j coordinate directions, respectively. p and ρ stand for the pressure and the mixture density. μ is the laminar viscosity of the fluid mixture.

It should be noted that the one-way coupling method is applied indicating that the particle movement is influenced by the continuous phase, but the flow phase is not influenced by the particle motion. So, there are no additional source terms in Eq. (3).

The fluid mixture properties of water and air in Eq. (3) are calculated as

$$\begin{aligned}\mu &= \alpha_a \cdot \mu_a + \alpha_w \cdot \mu_w \\ \rho &= \alpha_a \cdot \rho_a + \alpha_w \cdot \rho_w\end{aligned}\quad (4)$$

where subscripts *a* and *w* represent air and water, respectively.

To predict the turbulent viscosity μ_t , the standard *k-ε* turbulence model is used. The transport equations of turbulence kinetic energy *k* and the turbulence dissipation rate ϵ can be given as

$$\frac{\partial(\rho k)}{\partial t} + \frac{\partial(\rho k u_j)}{\partial u_j} = \frac{\partial}{\partial x_j} \left[\left(\mu + \frac{\mu_t}{\sigma_k} \right) \frac{\partial k}{\partial x_j} \right] + P_t - \rho \epsilon \quad (5)$$

$$\frac{\partial(\rho \epsilon)}{\partial t} + \frac{\partial(\rho \epsilon u_j)}{\partial u_j} = \frac{\partial}{\partial x_j} \left[\left(\mu + \frac{\mu_t}{\sigma_\epsilon} \right) \frac{\partial \epsilon}{\partial x_j} \right] + C_{\epsilon 1} P_t \frac{\epsilon}{k} - C_{\epsilon 2} \rho \frac{\epsilon^2}{k} \quad (6)$$

where μ_t is computed by $\mu_t = C_\mu \rho k^2 / \epsilon$ with $C_\mu = 0.09$, σ_k and σ_ϵ are the turbulent Prandtl number for *k* and ϵ , and their values are set as 1.3 and 1.0, respectively. The other two empirical constants are given as $C_{\epsilon 1} = 1.44$ and $C_{\epsilon 2} = 1.92$.

2.2. Disperse-phase tracking method

The interactions among the particles are neglected as the volume-based concentration of abrasive particles in the present cases is less than 10%. The so-called one-way coupling method is adopted to track the abrasive particles. As the diameters of the particles are small, the rotation motions of the abrasive particles are neglected. The forces acting on each particle include the drag force, the virtual mass force, and the pressure gradient force. The governing equation for each abrasive particle in the Cartesian coordinate form can be given as

$$\frac{du_p}{dt} = F_d(u - u_p) + F_{vm} + F_p \quad (7)$$

where u_p is the particle velocity and F_d is the drag force per unit particle mass, which can be calculated as

$$F_d = \frac{18\mu}{\rho_p d_p^2} \frac{C_D Re_p}{24} \quad (8)$$

where Re_p stands for the particle Reynolds number which defined as

$$Re_p = \frac{\rho_p d_p |u - u_p|}{\mu} \quad (9)$$

where d_p represents the particle diameter and ρ_p stands for the particle density. The drag coefficient C_D is predicted by the following equation [16]:

$$C_D = \frac{24}{Re_p} (1 + b_1 Re_p^{b_2}) + \frac{b_3 Re_p}{b_4 + Re_p} \quad (10)$$

where

$$\begin{cases} b_1 = \exp(2.3288 - 6.4581\varphi + 2.4486\varphi^2) \\ b_2 = 0.0964 + 0.5565\varphi \\ b_3 = \exp(4.905 - 13.8944\varphi + 18.4222\varphi^2 - 10.2599\varphi^3) \\ b_4 = \exp(1.4681 + 12.2584\varphi - 20.7322\varphi^2 + 15.8855\varphi^3) \end{cases} \quad (11)$$

where φ is termed as the shape factor to take the particle sphericity into consideration as shown in **Figure 2**. According to its definition, $\varphi = s/S$, where s represents the nominal surface area of a sphere particle which has the same volume as the real particle and S is the actual surface area of the particle; $\varphi = 1$ indicates that the particle is spherical, where φ is smaller than unity indicating that the particle is nonspherical. A smaller value of the shape factor represents an increase of the particle irregularity.

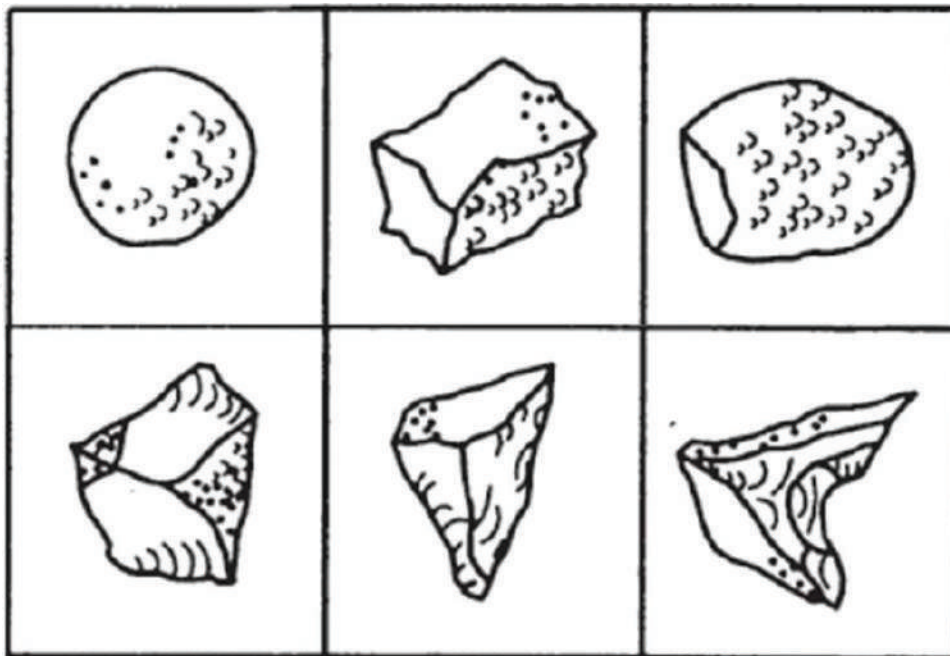


Figure 2. Typical shapes of abrasive particle [17].

The virtual mass force acting on each abrasive particle can be calculated as

$$F_{vm} = \frac{1}{2} \frac{\rho}{\rho_p} \frac{d}{dt}(u - u_p) \quad (12)$$

The effect of virtual mass is significant when the particle density ρ_p is much smaller than the fluid phase density ρ .

The pressure gradient force is caused by a pressure difference and can be modeled as

$$F_p = \frac{\rho}{\rho_p} \nabla p \quad (13)$$

The diameters of abrasive particles used in the present simulations are very small, and the pressure difference over one particle diameter distance can be ignored. Therefore, only the drag force is taken into consideration in the current study.

For turbulent flows, the fluid velocity can be divided into the mean velocity and the random fluctuation velocity. To predict the effect of turbulent flow velocity fluctuations on the particle movement, the random walk model (RWM) is used. The turbulent fluctuating velocity is modeled as

$$u' = \zeta \sqrt{\frac{2k}{3}} \quad (14)$$

where k is the calculated turbulence kinetic energy and ζ is a Gaussian distributed random number.

A reflecting boundary condition is adopted to consider the interactions between the abrasive particles and the wall boundaries. The particles reach the wall and change directions after the collisions. Two famous parameters, namely, the normal restitution coefficient e_n and the tangential coefficient e_τ , are defined as follows:

$$\begin{aligned} e_n &= \frac{v_{p2}}{v_{p1}} \\ e_\tau &= \frac{u_{p2}}{u_{p1}} \end{aligned} \quad (15)$$

where v_p is the particle velocity normal to the wall and the corresponding subscript 1 and 2 represent before and after the collision, respectively. Likely, the tangential coefficient accounts for the momentum changes in the direction tangential to the wall boundary. The restitution coefficients for both directions equal to unity indicate a fully elastic collision which means that there is no energy loss during the collision.

2.3. Computational model and numerical setup

A typical geometry of the three-dimensional AWJ nozzle is illustrated in **Figure 3**. The high-pressure water tube diameter is 4 mm, the orifice diameter is 0.4 mm, the mixing chamber

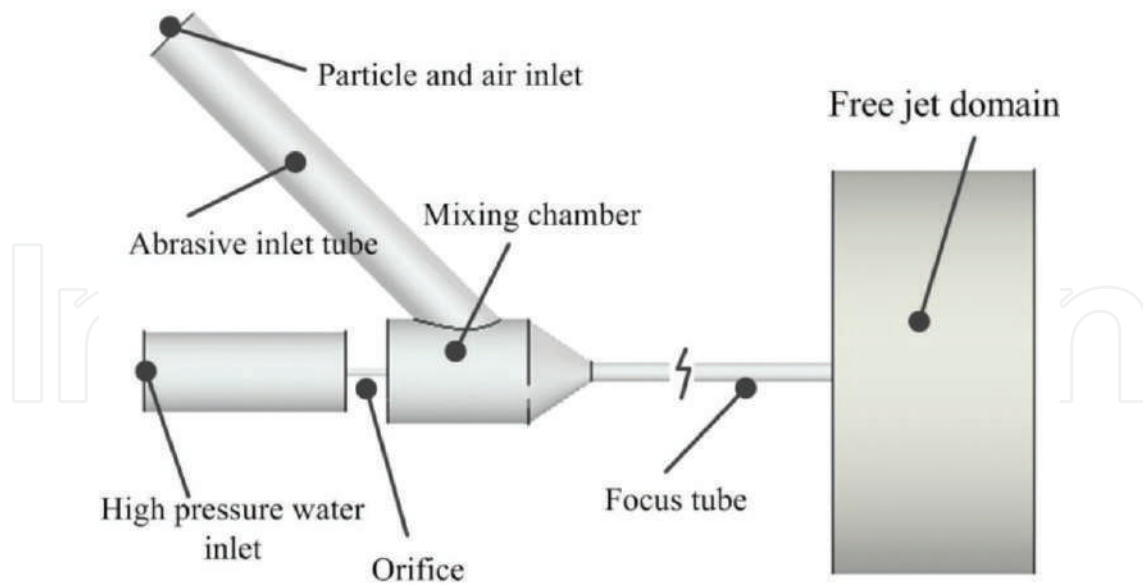


Figure 3. Geometry of the AWJ nozzle for the 3D simulation.

diameter is 5 mm, and the abrasive particle inlet tube diameter is 3 mm. The focus tube has a diameter of 1 mm with the length of 60 mm. Two AWJ nozzles with different abrasive inlet tube angles are modeled in the present study as illustrated in **Figure 4**. Model 1 represents the AWJ nozzle with the abrasive inlet tube angle of 45° , and model 2 stands for the AWJ nozzle with the abrasive inlet tube angle of 60° . The computational domains of the two models are meshed as shown in **Figures 5** and **6**. In order to ensure the accurate tracking of VOF surface, a mesh refinement is conducted around the orifice and the water-air interface regions. Both tetrahedral and hexahedral meshes are generated inside the computational domains, and high-density mesh regions are located where large gradients are expected. The grid independence analysis for both the two models indicate that the results predicted with the meshes with about 900,000 nodes will not change with further refinement of mesh resolution. The meshes used in the subsequent simulations are given in **Figures 5** and **6**.

The pressure inlet boundary condition with a given pressure of 300 MPa is specified at the water inlet, while atmospheric pressure is fixed at the air inlet boundary. At the free jet domain boundary region, the outlet boundary condition is applied with a pressure fixed at

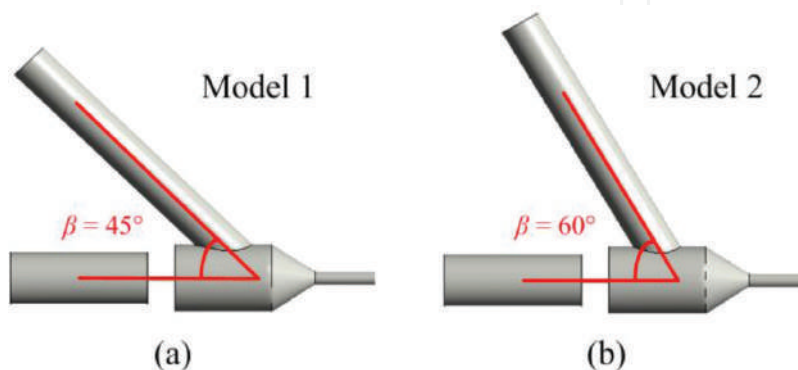


Figure 4. AWJ nozzles with different abrasive inlet tube angles.

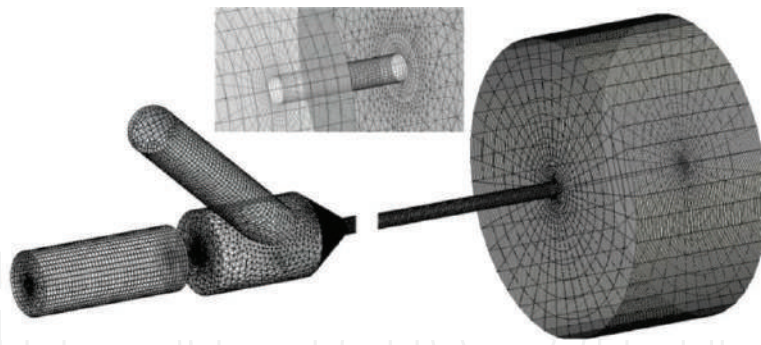


Figure 5. Computational mesh used in the simulations (model 1).

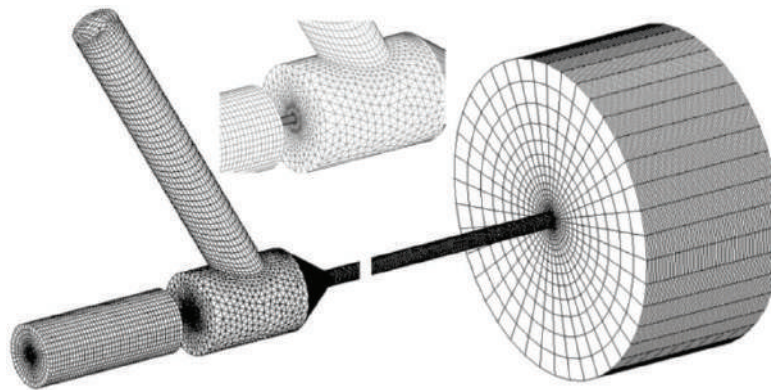


Figure 6. Computational mesh used in the simulations (model 2).

the atmospheric pressure. The no-slip wall boundary condition is specified at the walls. The abrasive particles are injected into the computational domains with uniform velocity with a given mass flow rate of 5 g/s. And, the density of abrasive particle is 2600 kg/m³. The interactions between the wall and particles are modeled by specifying the restitution coefficients. The abovementioned steady-state governing equations for air and water phases are finally discretized in space domain using the finite volume method (FVM) with SIMPLE algorithm. The QUICK scheme is used to approximate the phase volume fraction. The second-order accurate central differential scheme is adopted to discretize the diffusion terms. And, the second-order accurate upwind scheme is implemented to discretize the other convective terms. The convergence criterions for all the cases are specified as that the residuals for each equation drop below 10⁻⁴. Once the steady-state simulations of continuous phases are completed, the abrasive particles are released, and the particle trajectories are correspondingly predicted. All the simulations are performed with commercial software Ansys Fluent 15.0.

3. Results and discussion

3.1. Flow field inside AWJ nozzle

Figure 7 shows the predicted flow patterns inside the two AWJ nozzles at the same operating pressure of 300 MPa. The typical free jet structures are captured by the present model in the

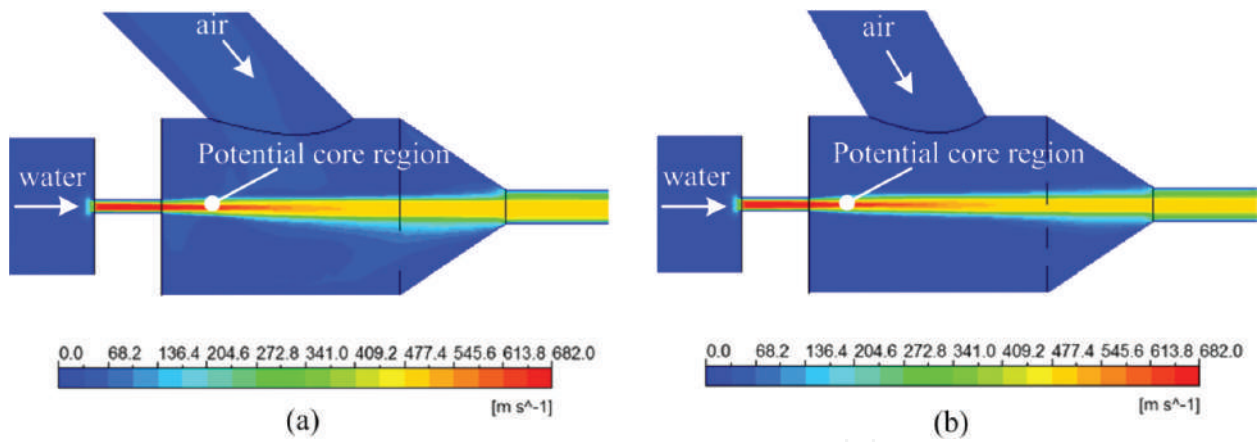


Figure 7. Velocity contour inside (a) model 1 and (b) model 2 AWJ nozzles.

mixing chamber. It can be seen that the high-pressure water ejected from the orifice produces a high-speed water jet. The predicted potential core region has the maximum velocity, and the axial velocity begins to decay significantly further downstream. Due to the high-speed region in the chamber, a comparatively low-pressure region is generated, and thus the air is entrained into the nozzle by the water jet entraining effect. The predicted area-weighted average velocity at the air inlet is about 37 m/s. It is noted that the comparatively low-velocity region in the velocity is slightly asymmetric, which is mainly caused by the presence of the particle inlet tube. The velocity distributions in the axial lines of the two types of nozzles are shown in Figure 8. There is a small gap between the velocity profiles in the mixing chamber. However, the two lines are almost collapsed together in the focus tubes. Generally, the impact of abrasive inlet tube angle on the fluid flow is not significant.

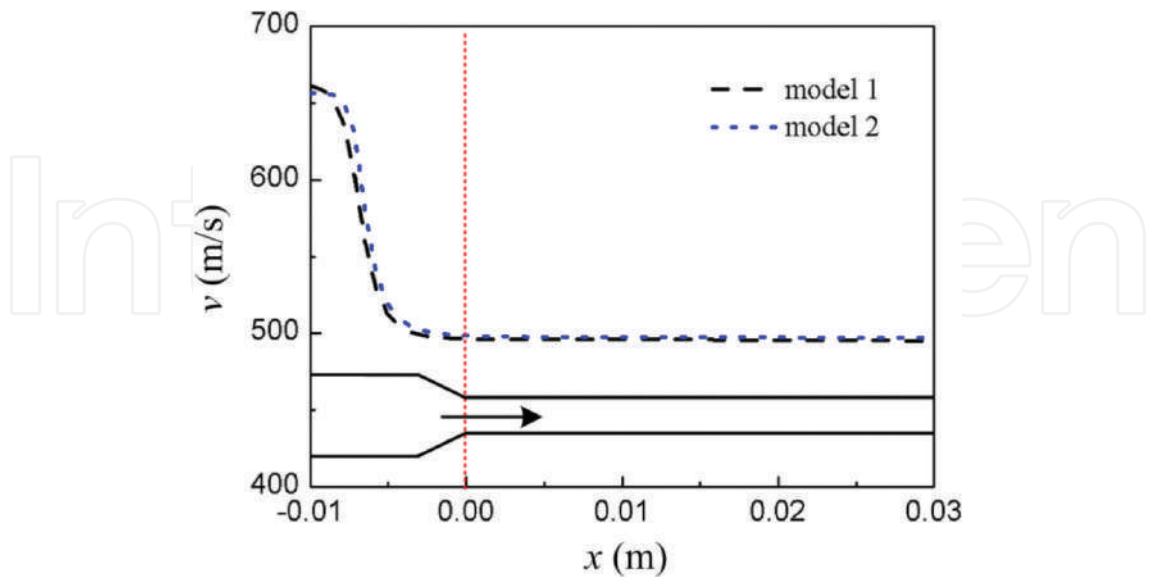


Figure 8. Velocity distributions in the axial lines of the two nozzles.

3.2. Independence analysis of particle number

As the abrasive particle concentrations on the volume fraction basis are less than 1% in the present simulations, the one-way coupling method is utilized to predict the particle trajectories, and the effects of particle movements on the continuous phases are not considered. Thus, the integration of particle paths is a post-process, which is performed after the fluid field is obtained. Since the effect of turbulent velocity on the particle paths has been accounted, the independence analysis of particle number should be conducted in order to obtain statistically representative results.

Four different particle numbers are sampled at about 60 different cross sections along the focus tube, and the results are shown in **Figure 9**. It should be noted that the particles are assumed to be spherical, and the energy loss due to particle-wall interactions is also neglected. As illustrated in **Figure 9**, the sampled particle velocities tend to collapse together with the increasing of sampled particle numbers. It is noted that when the sampled particle number is greater than 10,500, the resulted velocities do not change with further increase of sampled particles. Thus, the tracked particle number is maintained at about 10,500 in the subsequent calculations.

3.3. Effect of particle initial velocity

The particle initial velocities at the abrasive particle inlet tube are hard to determine experimentally, and thus in the abovementioned simulations, the initial velocity is set as zero uniformly, and the particles are accelerated by the entrained air phase. In order to ensure that the boundary condition for the inlet abrasive particle is reasonable, the effects of particle initial velocities on the final predicted velocities need to be further investigated. Two

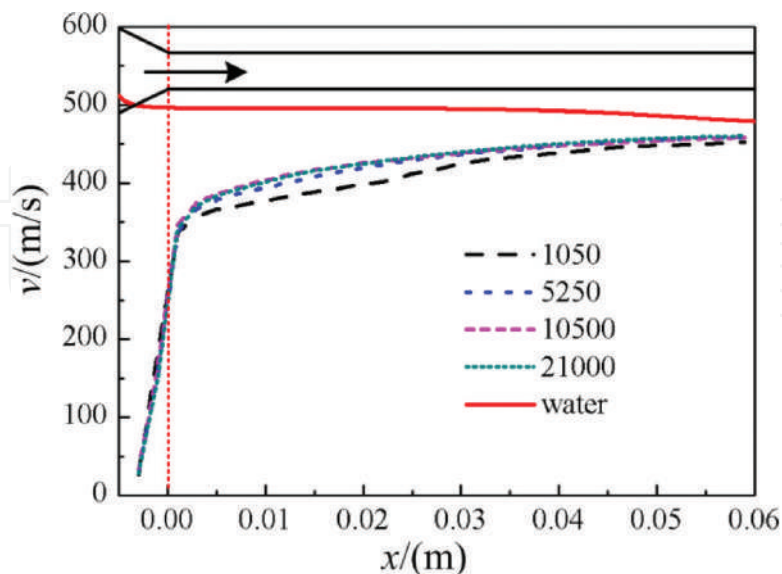


Figure 9. Velocity distribution with different particle sampling numbers (model 1).

different particle initial velocities for the two nozzles are discussed, and the sampled results are given in **Figure 10**. As it can be seen, the predicted velocities under the two different particle initial velocities coincide with each other for each model. Thus, it is confirmed that the simulated results are insensitive to the particle initial velocities within the discussed range of 0–2 m/s.

The results also indicate that the general particle accelerations for both the two AWJ nozzle models are similar. In the convergence section of the focus tubes, the particle velocities are increased linearly with the increase of the axial distance, and the velocity rises sharply from a low-level value to a high-level value. In the initial straight part of the focus tubes, the accelerations of abrasive particles are gradually weakened, and the overall velocities are approaching a constant value which is always smaller than the corresponding water speed. As the particles move further downstream in the focus tube, the velocity differences between the water and the particle are further reduced, which means that the particles are continuously accelerated by the high-speed jet flow. As shown in **Figure 10**, the velocity profiles of model 1 and model 2 have a gap in the initial section of the focus tube. The particle acceleration of model 2 is faster than that of model 1, which indicates that a larger abrasive particle inlet tube angle can enhance the particle accelerations.

3.4. Effect of shape factor

The shape factor in the drag coefficient model is introduced to account for the effects of particle shape on the drag force predictions. Two different shape factors are defined for both the two nozzle models to investigate the shape factor value on the calculated particle velocities. As given in **Figure 11**, the particle velocities under with the two different shape factors show obvious differences for both model 1 and model 2. At the convergence part of the focus tube, the corresponding two velocity curves for each nozzle model collapse together. However, at

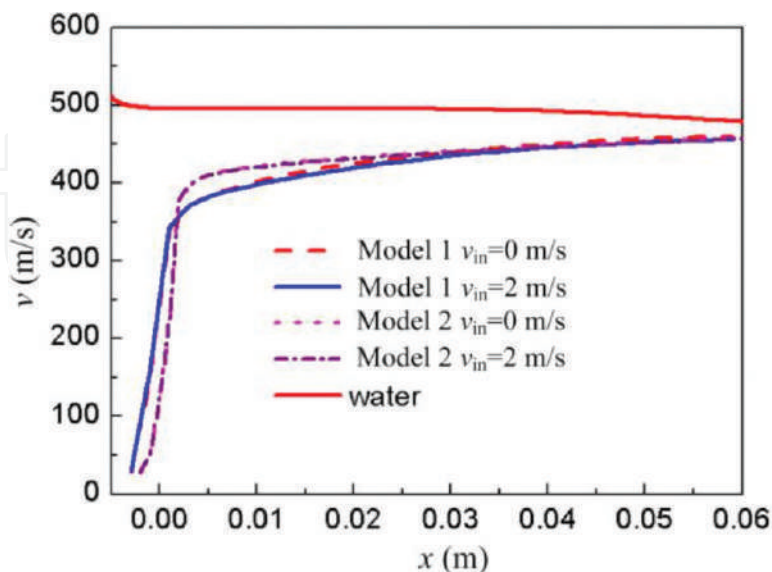


Figure 10. Velocity distributions with different particle initial velocities.

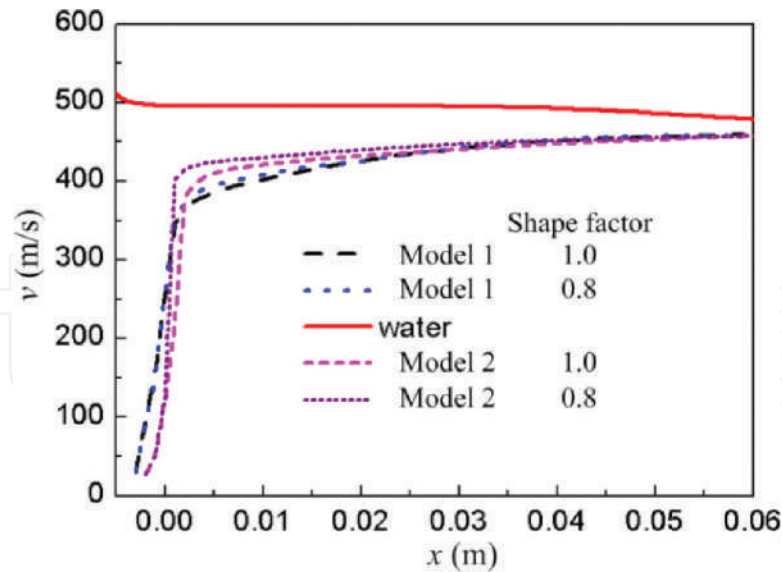


Figure 11. Velocity distributions with different shape factors.

the straight part between 0.0 and 0.04 m, the curves begin to separate, and the velocity with smaller shape factor is comparatively larger. It can be explained by the fact that the drag forces acting on the abrasive particles are larger at a smaller shape factor and thus the particles are accelerated much more quickly. At the following part, the curves again come together indicating that the particle velocities under the selected shaper factors are the same at the focus tube outlet. Thus, the results further reveal that the length of focus tube has an impact on the final particle velocities and a properly designed focus tube should be introduced to ensure that the abrasive particles are fully accelerated.

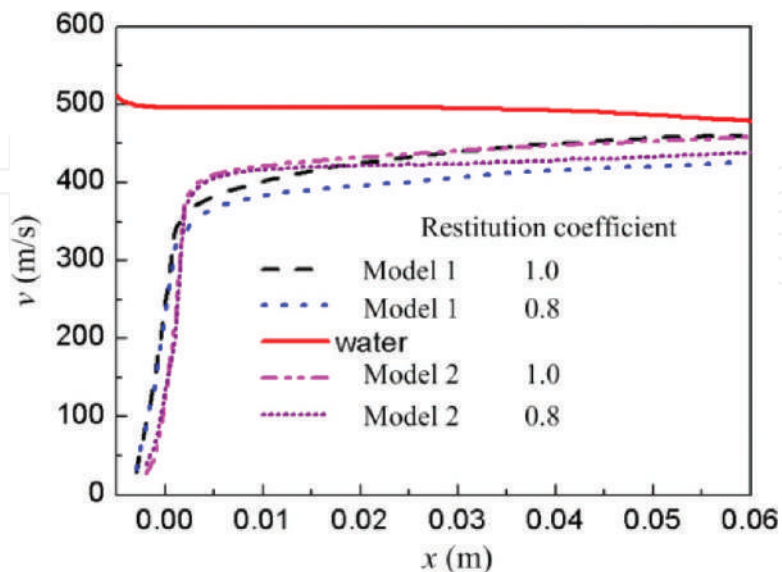


Figure 12. Velocity distributions with different restitution coefficients.

3.5. Effect of particle-wall restitution coefficient

The effects of restitution model accounting for the particle-wall interactions on the predicted velocities are studied to obtain an accurate prediction on the particle paths. When the restitution coefficients at normal and tangential directions are both set as unity, the particle energy loss upon collision is neglected. In real cases, the rebound velocity is lower than the incident velocity. In this work, two kinds of restitution coefficients for both the two AWJ nozzle models are adopted, and the predicted results are shown in **Figure 12**. With the decreased restitution coefficients, the sampled particle velocities at the straight section of the focus tube are lower for both the two models, which indicate that a proper rebound model should be introduced in order to consider the real behaviors of particle-wall interactions.

4. Conclusions

The multiphase flows inside the two AWJ nozzle models with different abrasive inlet tube angles at the same operating pressure are simulated using the standard $k-\varepsilon$ turbulence model coupled with the VOF multiphase model based on the Euler-Lagrangian approach. The results indicate that sufficient particles should be sampled in order to obtain a statistically representative result. At the studied velocity range, the particle initial velocities for the two AWJ nozzles do not influence the predicted results. Further analysis shows that for both the two nozzles smaller particle shape factors enhance the process of particle accelerations and a proper length of the focus tube can guarantee that the particles will be fully accelerated. The restitution coefficients may have a significant influence on the particle paths as well as the predicted particle velocities. And, a proper rebound model should be introduced in order to capture the real particle behaviors in the AWJ nozzle. The abrasive inlet tube angle has little impact on the water-phase flows, while a larger abrasive inlet tube angle can enhance the particle accelerations.

Acknowledgements

This work was financially supported by the National High-Technology Research and Development Program 863 (2015AA043401).

Author details

Xinping Long^{1*} and Qi Liu²

*Address all correspondence to: xplong@whu.edu.cn

1 School of Power and Mechanical Engineering, Wuhan University, Wuhan, Hubei, China

2 China Ship Development and Design Center, Wuhan, China

References

- [1] Matsumura T, Muramatsu T, Fueki S. Abrasive water jet machining of glass with stagnation effect. *CIRP Annals – Manufacturing Technology*. 2011;**60**:355-358
- [2] Wang J, Shanmugam DK. Cutting meat with bone using an ultrahigh pressure abrasive waterjet. *Meat Science*. 2009;**81**:671-677
- [3] Henning A, Liu HT, Olsen C. Economic and technical efficiency of high performance abrasive waterjet cutting. *Journal of Pressure Vessel Technology*. 2012;**134**:021405-021405
- [4] Haghbin N, Ahmadzadeh F, Spelt JK, Papini M. Effect of entrained air in abrasive water jet micro-machining: Reduction of channel width and waviness using slurry entrainment. *Wear*. 2015;**344-345**:99-109
- [5] Axinte DA, Srinivasu DS, Kong MC, Butler-Smith PW. Abrasive waterjet cutting of polycrystalline diamond: A preliminary investigation. *International Journal of Machine Tools and Manufacture*. 2009;**49**:797-803
- [6] Long X, Ruan X, Liu Q, Chen Z, Xue S, Wu Z. Numerical investigation on the internal flow and the particle movement in the abrasive waterjet nozzle. *Powder Technology*. 2017;**314**:635-640
- [7] Momber AW. Energy transfer during the mixing of air and solid particles into a high-speed waterjet: An impact-force study. *Experimental Thermal and Fluid Science*. 2001;**25**:31-41
- [8] Liu H, Wang J, Kelson N, Brown RJ. A study of abrasive waterjet characteristics by CFD simulation. *Journal of Materials Processing Technology*. 2004;**153-154**:488-493
- [9] Lee J-H, Park K-S, Kang MC, Kang BS, Shin BS. Experiments and computer simulation analysis of impact behaviors of micro-sized abrasive in waterjet cutting of thin multiple layered materials. *Transactions of Nonferrous Metals Society of China*. 2012;**22**(3):s864-s869
- [10] Shanmugam DK, Masood SH. An investigation on kerf characteristics in abrasive waterjet cutting of layered composites. *Journal of Materials Processing Technology*. 2009;**209**:3887-3893
- [11] Coray PS, Jurisevic B, Junkar M, Heiniger KC. Measurements on 5:1 scale abrasive water jet cutting head models, In: *Proceedings of the 6th International Conference on Management of Innovative Technologies MIT 2003 – post-conference edition*. Ljubljana: University of Ljubljana; 2003. pp. 87-102
- [12] Yang M, Wang Y, Kang C, Feng YU. Multiphase flow and wear in the cutting head of ultra-high pressure abrasive water jet. *Chinese Journal of Mechanical Engineering*. 2009;**22**:729-734
- [13] Basha AT, Annoni M, Monno M, et al. Investigation of the hydrodynamic characteristics of abrasive water jet cutting head[J]. *International Journal of Machining & Machinability of Materials*. 2013;**14**(1):105-122

- [14] Tazibt A, Parsy F, Abriak N. Theoretical analysis of the particle acceleration process in abrasive water jet cutting. *Computational Materials Science*. 1996;5:243-254
- [15] Ahmed SE, Naser J, et al. Numerical Simulation of Abrasive Water Jet for Different Taper Inlet Angles, [C]//14th Australasian Fluid Mechanics Conference, Australia. 2001:645-648
- [16] Haider A, Levenspiel O. Drag coefficient and terminal velocity of spherical and non-spherical particles. *Powder Technology*. 1989;58:63-70
- [17] Momber AW, Kovacevic R. *Principles of Abrasive Water Jet Machining*. London: Springer; 1998

IntechOpen

We are IntechOpen, the world's leading publisher of Open Access books Built by scientists, for scientists

6,300

Open access books available

171,000

International authors and editors

190M

Downloads

Our authors are among the

154

Countries delivered to

TOP 1%

most cited scientists

12.2%

Contributors from top 500 universities



WEB OF SCIENCE™

Selection of our books indexed in the Book Citation Index
in Web of Science™ Core Collection (BKCI)

Interested in publishing with us?
Contact book.department@intechopen.com

Numbers displayed above are based on latest data collected.
For more information visit www.intechopen.com



Ultrasonic Machining: A Total Mechanical Machining Technology Using Loose Abrasive Particles

Jingsi Wang

Additional information is available at the end of the chapter

<http://dx.doi.org/10.5772/intechopen.75170>

Abstract

Although manufacturing technologies are well developed for materials like metals and their alloys, considerable problems still exist in the fabrication of hard and brittle materials including ceramics and glass. Their superior physical and mechanical properties lead to long machining cycle and high production cost. Ultrasonic machining (USM) using loose abrasive particles suspended in a liquid slurry for material removal is considered an effective method for manufacturing these materials. This work gives a brief overview of USM first and then mainly addresses the development of a simulation model of this process using a mesh-free numerical technique, the smoothed particle hydrodynamics (SPH). The crack formation on the work surface impacted by two abrasive particles is studied for understanding the material removal and the interaction of abrasive particles in USM. Experiments are also conducted to verify the simulation results. The SPH model is proven useful for studying USM and is capable of predicting the machining performance.

Keywords: ultrasonic machining, smoothed particle hydrodynamics (SPH), hard and brittle materials, material removal mechanism, hole drilling

1. Introduction

Hard and brittle materials, such as glass, ceramics, and quartz crystal, are getting more and more attention in the recent years due to their superior properties like high hardness, high strength, chemical stability, and low density. High-performance products made of these materials play an important role in various industrial fields including semiconductor, optical components, aerospace, and automotive industries [1, 2]. However, considerable problems such as long machining cycle and high production cost still exist in the fabrication of hard and brittle materials. Particular difficulties are the production of micro-/nanostructures with

high machining efficiency, high aspect ratios, and good surfaces possessing no residual stress and microcracks. Hence, there is a crucial need for developing precision and efficient micro-machining techniques for these materials.

Nontraditional machining techniques such as electric discharge machining and laser beam machining have been proposed to machine hard and brittle materials. However, even these processes have prominent limitations that the machined surfaces are always subjected to heat-induced damages like recast layer and thermal stress. Ultrasonic machining (USM) is another alternative method for manufacturing both conductive and nonconductive hard and brittle materials. It is known as a total mechanical process without suffering from heat or chemical effects, so USM would not thermally damage the machining objects or appear to cause significant levels of residual stress and chemical alterations.

However, not much research has been conducted to clarify the mechanism of USM up to date, and the knowledge for the process is far from sufficient to provide a complete understanding and instructive rules for practical use. Therefore, no further developments of micro-USM happened in recent years. In this work, a brief overview of USM is given first in Section 2. Then, a mesh-free numerical technique, the smoothed particle hydrodynamics (SPH), is introduced to simulate the USM process in Section 3, and its verification experiments are presented after that. The crack formation on the work surface impacted by two abrasive particles was studied in the simulation to reveal the material removal and the interaction of abrasive particles in USM. Finally, problems to be solved in order to put USM into an effective industrial micro-machining method are given. Further work should be conducted to clarify the nature of USM process for improving the machining performance.

2. Overview of ultrasonic machining (USM)

2.1. Principle of USM

Figure 1 shows a schematic of the basic elements of a USM apparatus used nowadays. High-frequency electrical energy can be converted into mechanical vibrations with resonant frequency via the transducer. The excited vibration is subsequently transmitted through an energy-focusing horn to amplify the vibration amplitude and finally delivered to the tool tip. Thus, the tool which locates directly above the workpiece can vibrate along its longitudinal axis with a desired high amplitude. A slurry comprising hard abrasive particles (generally using silicon carbide, boron carbide, and alumina) in water or oil is provided constantly into the machining area. During the fabrication of hard and brittle materials, a large number of tiny fractures occur on the work surface and lead to the material removal.

2.2. Features and potentialities of USM

Markov [3] classified workpiece materials into three categories in consideration of the USM suitability: the materials belonging to the first group, such as glass, mica, and quartz, are quite brittle and easy for USM process. The materials are removed by the initiation and propagation

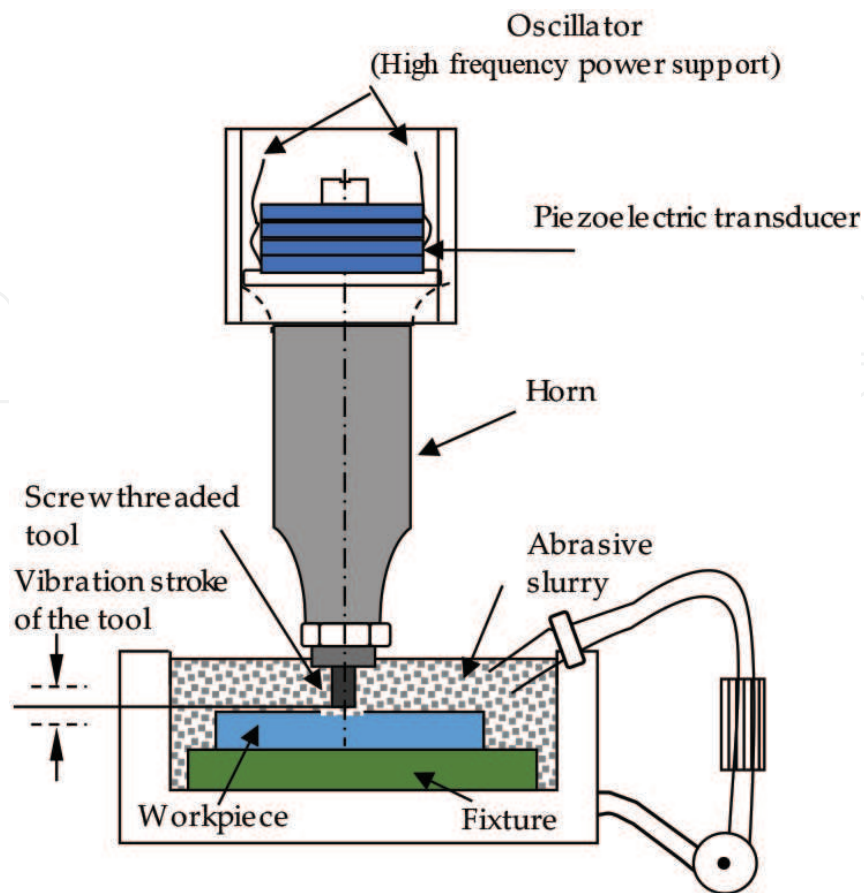


Figure 1. Schematic of basic elements in USM.

of tiny cracks of the workpiece in this situation. The second group includes the materials that exhibit some plastic deformation before fracture like titanium alloys, carburized, and nitrided steels. USM can machine these materials although with some difficulty. The last group consists of the ductile materials, such as soft steel and copper, and they are unsuitable in principle for USM. Note that a recent research reported that the ductile substrate materials are not really removed but are displaced, which also have been observed for some fine polishing operations [4]. The classification of the materials and fields of application for USM are given in **Table 1**.

USM has shown potentialities in many manufacturing uses; the most commonly ones are the fabricating structures of any shapes on hard and brittle materials. Hole drilling always stands as the most popular machining process for product manufacturing, and USM in particular shows a high potentiality in fabricating diverse holes either with large/small diameters or high aspect ratios. Masuzawa's group firstly proposed micro-USM as an effective micromachining process for hard and brittle materials. Holes with diameters as small as $5\ \mu\text{m}$ and aspect ratios larger than 5 were successfully fabricated on quartz glass and silicon by micro-USM in one of their studies [6]. At the other extreme, tools with diameters as large as 85 mm were successfully employed for drilling holes with a high-capacity (2.5 kW) ultrasonic machine [7]. Besides, USM is playing an irreplaceable role in fabricating holes with a high

Group of material	Predominant type of deformation	Type of failure	Field of application of USM
I. Glass, mica, quartz, ceramic, diamond, germanium, silicon, ferrite, alsifer	Elastic	Brittle	Manufacturing parts of semiconducting materials Making industrial diamonds Fabricating special ceramics Manufacturing parts of glass quartz or minerals in the optical and jewelry industries Machining ferrite, alsifer, and other materials
II. Alloys tempered to high hardness carburized and nitrided steels, titanium alloys	Elastic-plastic	Brittle after work hardening by plastic deformation	Making and repairing hard alloy dies, press tools, and purchases Shaping or sharpening hard alloy tools
III. Lead, copper, soft steel	Plastic	No failure (or ductile failure)	Unsuitable for ultrasonic machining

Table 1. Classification of materials and fields of application for USM [3, 5].

aspect ratio. Micro-holes under 100 μm in diameter and aspect ratios of 10 on quartz glass were achieved by electrorheological fluid-assisted USM [8].

There also has been a heavy industrial demand for the fabrication of 3D microstructures on various hard and brittle materials. Two ways are used to achieve microstructures on hard and brittle materials via USM. One is by directly duplicating the tool shape on workpiece. In this way, complex 3D structures or multiple holes can be generated with a single pass of the machining tool. However, some problems including different machining rates over the whole working area and differential tool wear rate should be solved when using tools of complex form for keeping the product shape [9, 10]. Moreover, it is troublesome to fabricate micro-tools of complex shapes. The other one is to employ a simple “pencil” tool and contour the complex structures via a computerized numerical control (CNC) program. By using this method, machining any complex microstructures on hard and brittle materials accurately is possible. Sun et al. [11] have developed a 3D micro center-pin bearing air turbine using this method successfully, and the test results show that the turbine has a great reliability.

2.3. Involved material removal mechanism

The material removal mechanisms in basic USM were investigated quite intensively. Three well-recognized major removal actions were summarized by the previous researchers and include [5, 9, 12] (i) mechanical abrasion due to direct hammering of larger abrasive particles on the workpiece surface, (ii) microchipping resulted from the impact of free-moving abrasive particles, and (iii) cavitation erosion from the abrasive slurry. These mechanisms are schematically shown in **Figure 2**.

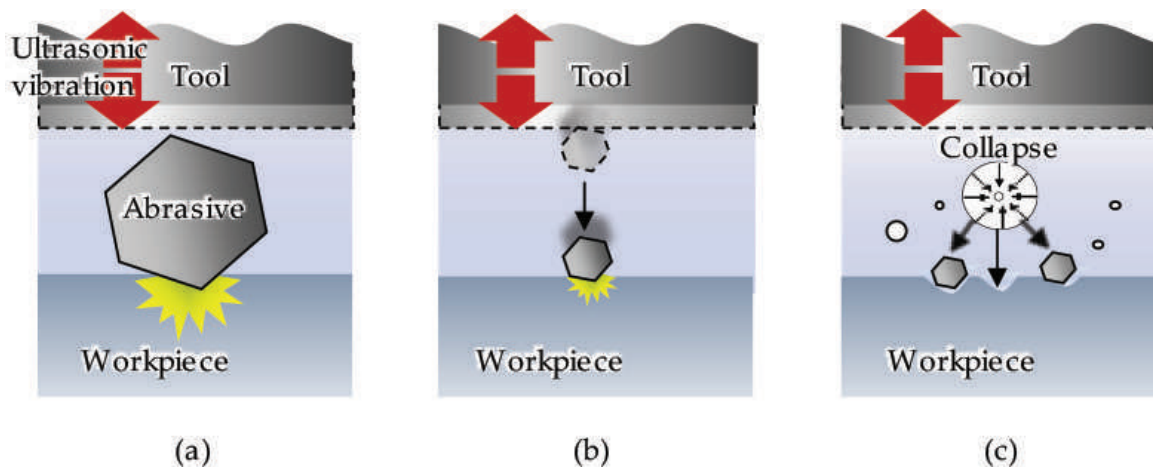


Figure 2. Schematic diagram of material removal mechanisms in USM: (a) hammering action, (b) impact action, and (c) cavitation erosion.

However, as it is difficult to observe the USM phenomena directly, a total understanding of the material removal is still not possible. Only qualitative evaluations according to experimental results were reported [13–15], except that an analysis model was established recently [16] based on the former study [17]. In other studies, the researchers concentrated on revealing the material removal mechanism [5, 18] by assuming the hammering of an abrasive particle in USM as an indentation process. However, the direct indentation process does not involve the actions including the tool vibration and abrasive fracture in USM; a more effective way for investigating and understanding the nature of material removal in USM is necessary.

The present author's group firstly proposed to study the influences of the hammering action and the impact action on material removal in USM process using a mesh-free numerical simulation method, smoothed particle hydrodynamics (SPH) [19]. The results are shown in **Figures 3** and **4**, respectively. One cycle of the tool vibration was simulated, and the fluid effect was not considered. Fractures occurred in both the abrasive and the workpiece after the hammering action as shown in **Figure 3(d)**. However, in the case of impact action, the accelerated abrasive due to the tool impact did not generate fractures and rebounded as depicted in **Figure 4(d)**, which means that the impact action is not effective for material removal on the raw work surface. The obtained results support the common view that hammering action plays a primary role in material removal of USM process [5].

2.4. Main process parameters

A large number of input parameters exist in USM process which would influence the machining performance. A cause and effect diagram to show the potential factors affecting USM is depicted in **Figure 5**. Influences of major process parameters on the material removal rate, machining precision, surface quality, and tool wear have been widely experimentally investigated.

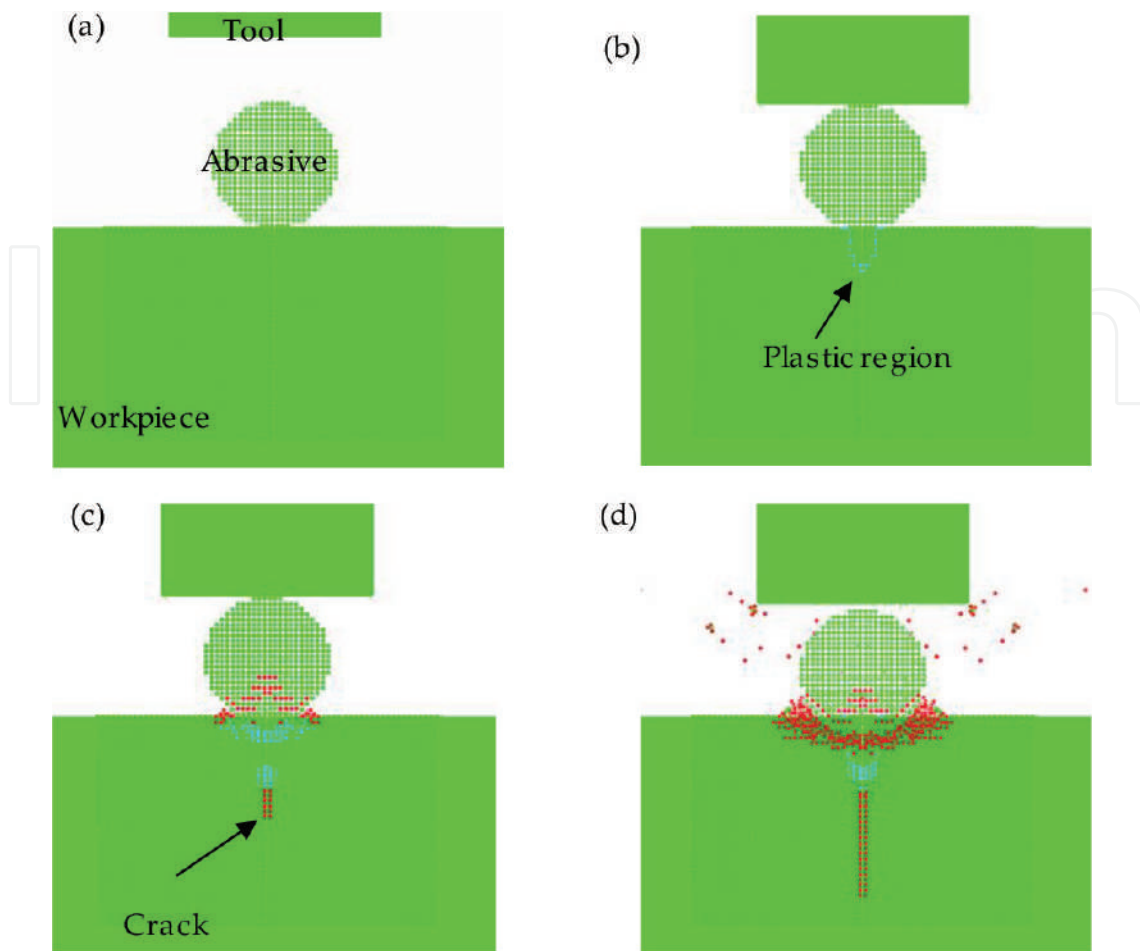


Figure 3. Simulation results of direct hammering action on the work surface: (a) before calculation, (b) after tool impact ($0.1 \mu\text{s}$ calculation), (c) $1 \mu\text{s}$ calculation, and (d) after unloading.

Lee and Chan [18] investigated the influence of vibration amplitude, static load, and the particle size on the machining rate and surface roughness. They suggested that the material removal rate (MRR) would be increased, while the machined surface would be roughened with any increase in these parameters. Yu et al. [20] stated that the machining speed decreased with an increase in the static load beyond a certain level and the abrasive size was a dominant factor influencing the surface roughness in USM. Guzzo et al. [21] demonstrated an increase in material removal rate with larger abrasive particles due to the increase in the stress induced by the impact of these particles against the work surface. Komaraiah and Reddy [5] discussed the effects of mechanical properties of the workpiece on material removal rate and found that the hardness and fracture toughness of the workpiece material played an important role in ultrasonic machining. There was a reduction in material removal rate with the increase of the hardness and fracture toughness of the workpiece material. In another study of Komaraiah and Reddy [22], experiments were carried out to clarify the effect of tool materials on the material removal rate, tool wear, and surface quality. While a difficult-to-machine material can be machined effectively, the tool in USM was

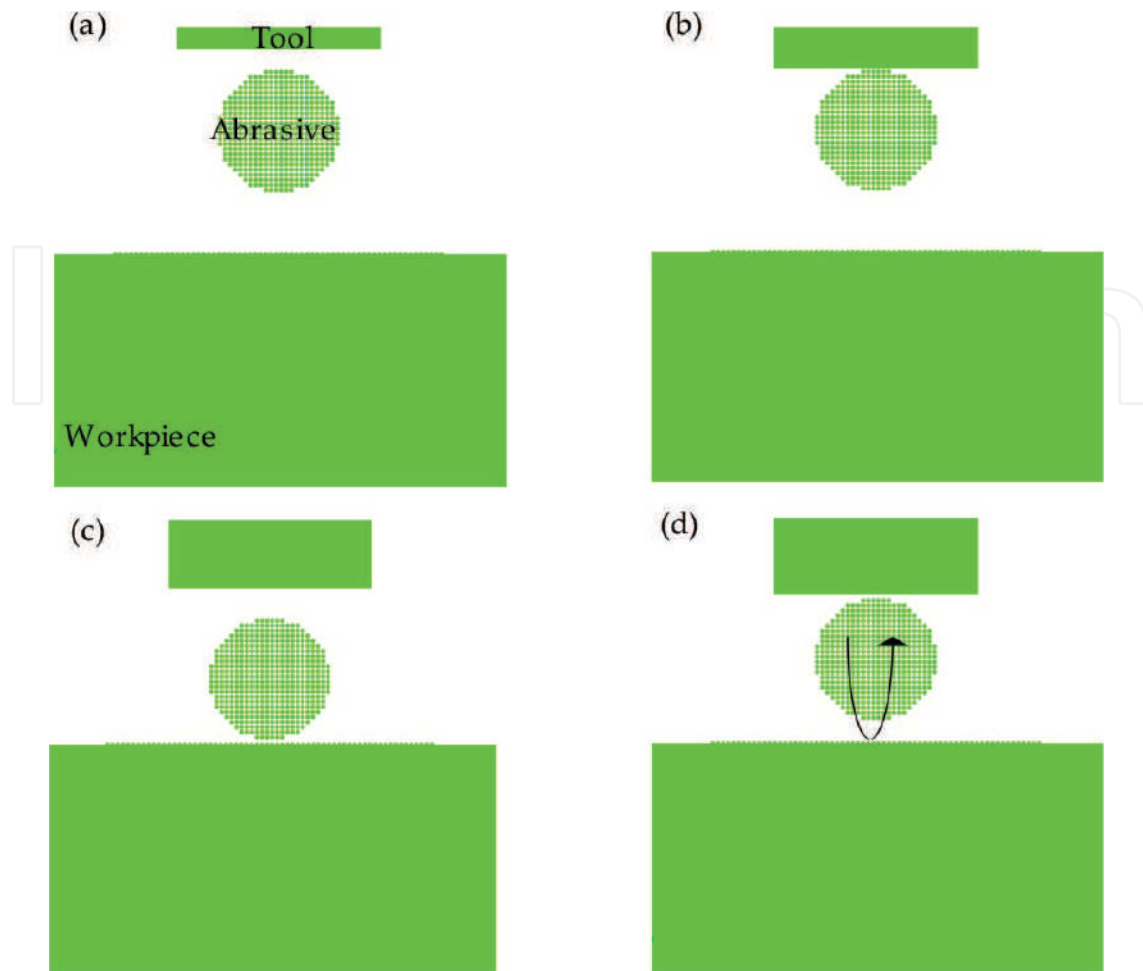


Figure 4. Simulation results of impact action: (a) before calculation, (b) after the tool impact on the abrasive particle, (c) after the particle impact on the work surface, and (d) rebound of the abrasive particle.

also worn. It was found that larger material removal rate, diametral tool wear resistance, and lower surface roughness can be obtained when using harder tool material. They also stated that both the hardness and the impact strength of the tool material would influence the longitudinal tool wear. Hocheng et al. [23] considered that large vibration amplitude increased the kinetic energy of abrasive particles, which wore the tool tip seriously, while a large static load depressed the free vibration of the abrasive particles and slowed down the tool wear.

Although many factors affect the machining performance of USM, it is believed that an optimum machining condition can be found to meet specific machining requirements. Further studies on the material removal mechanism in USM are extremely significant for understanding the influences of various process parameters on machining performance, which can provide a guidance in choosing suitable machining conditions and improve the machining performance.

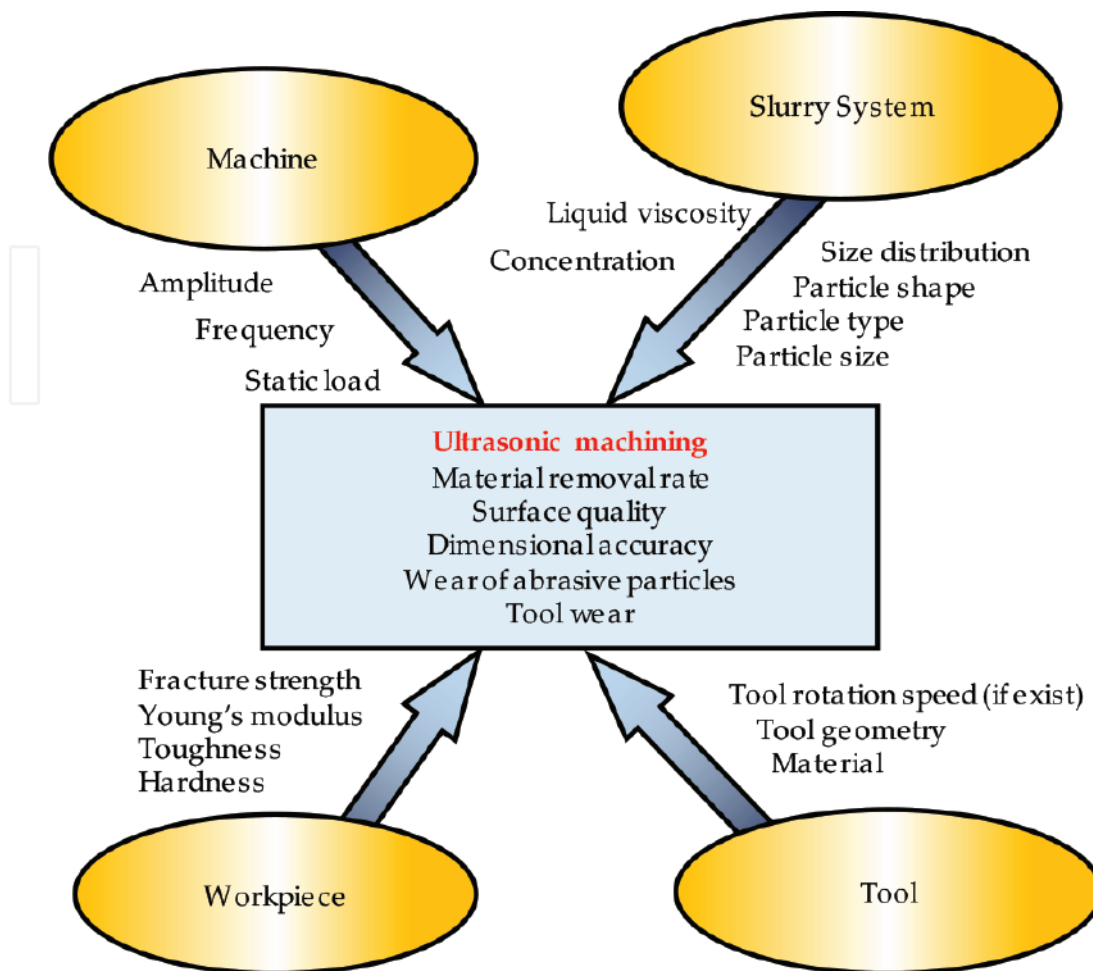


Figure 5. A cause and effect diagram for machining parameters in USM.

3. SPH simulation and experimental verification

3.1. Simulation method and results

3.1.1. Smoothed particle hydrodynamics (SPH)

SPH is a mesh-free numerical technique first introduced to solve astrophysics problems. In SPH, the system is represented by a set of particles that carry material properties and interact with each other according to the governing conservation equation. Problems involved in large deformation, which may cause errors due to mesh distortion and tangle with the grid-based method, can be effectively solved by the SPH. Thus, it is capable to simulate a USM process, in which material fracture occurs under repeated impacts of abrasive particles.

3.1.2. Material modeling

Glass, silicon carbide (SiC), and SS304 referred to stainless steel (AISI:304) were used for work-piece, abrasive, and tool material, respectively. Glass and SiC, which are hard and brittle, have

high compressive strength but low tensile strength; the Mie-Grüneisen polynomial equation of state was employed. On the other hand, the strength and damage behavior of these materials were modeled with Johnson-Holmquist material model [24, 25], in which fracturing occurs when the hydro tensile limit is reached. For SS304 material, the Shock equation of state was used, and the strength is formed by Steinberg-Guinan model. The constants related to the equations of the material models and material properties, for glass [26], SiC [27], and SS304 [28], are obtained from existing test data and summarized as shown in **Table 2**.

3.1.3. Modeling conditions and assumptions

In USM, a large number of abrasive particles act on the workpiece simultaneously by repeated impacts of the tool, and the hammering action dominates the main material removal. Therefore, the simulation model was built with two abrasive particles based on the direct hammering action to figure out influences of the interaction between adjacent abrasive particles on the process. **Figure 6** shows a snapshot of the model. The dimensions for each part is as defined in the figure. One half of the geometry was established with symmetric boundary conditions, and spherical abrasive particles were considered. The abrasive particle and the partial workpiece areas around the hammering site, where heavy deformation can occur, were built with SPH solver. The ultrasonically vibrated tool and the remaining parts of the workpiece were modeled by using the Lagrange finite element mesh. It is because that the SPH algorithm takes more time to find neighboring particles, which is usually more expensive in computation time. Materials in small deformation to be constructed with the grid-based Lagrange solver are helpful to reduce the calculation amount.

Figure 7 shows the moving conditions of the tool tip. The solid curve is the ideal condition given in the experiments: the tool tip vibrates sinusoidally with a frequency of 61 kHz and the total amplitude of 4 μm . Contrastingly, the dashed curve is the simplified condition for the calculation: the

	Float glass	SiC	SS304
Equation of state	Polynomial		Shock
Density (g/cm^3)	2.53	3.215	7.9
Bulk modulus (GPa)	45.4	220	None
Grüneisen coefficient (Γ)	None		1.93
Strength	Johnson-Holmquist		Steinberg-Guinan
Shear modulus (GPa)	30.4	193.5	77 (G_0)
Hugoniot elastic limit (GPa)	5.95	11.7	None
Yield stress (MPa)	None	None	340 (Y_0)
Failure	Johnson-Holmquist		None
Hydro tensile limit (MPa)	150	750	None

Table 2. Material models and relevant parameters.

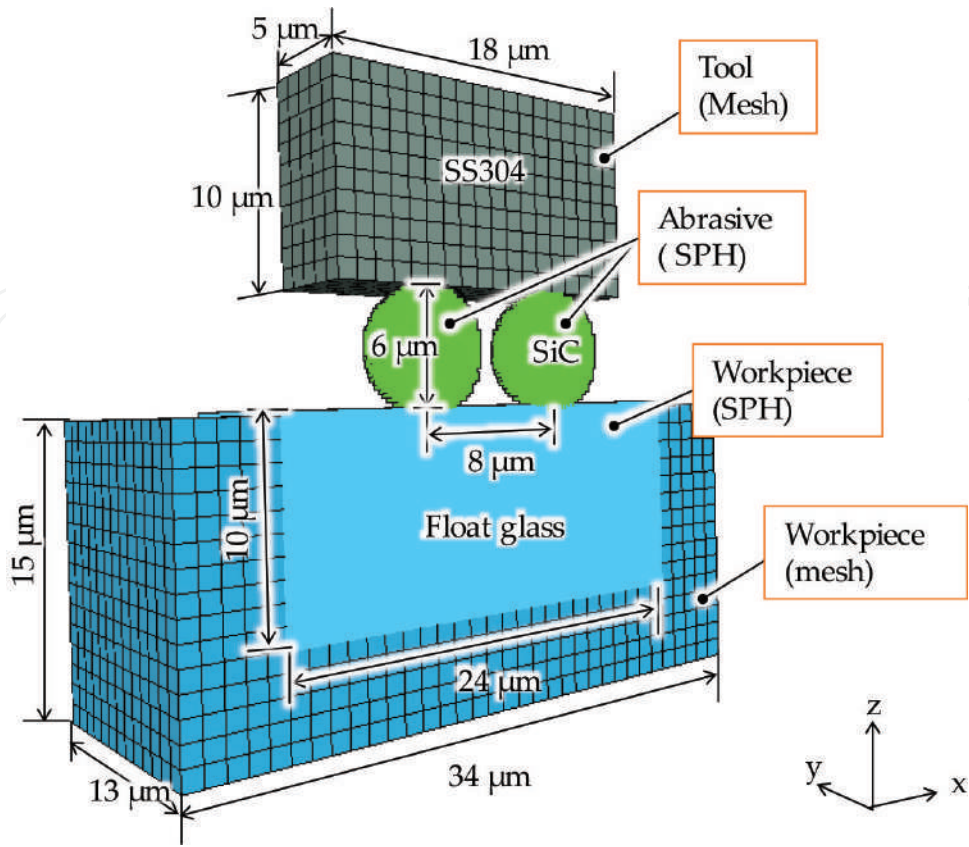


Figure 6. Snapshot of the initial state of the simulation model for two abrasive particles.

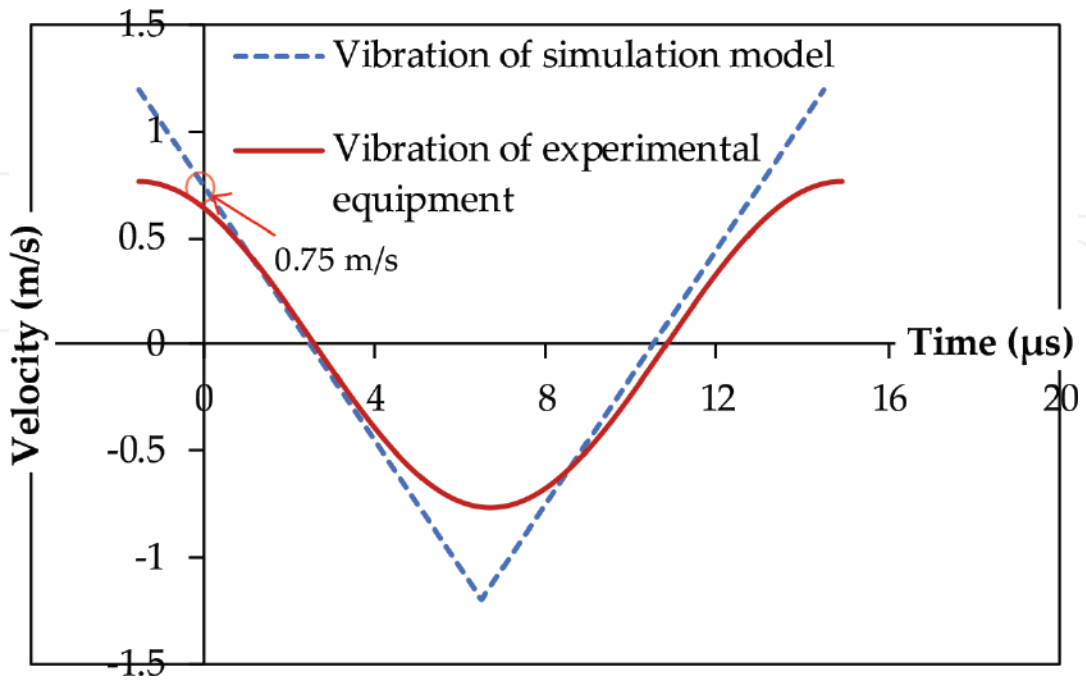


Figure 7. Velocity condition of the ultrasonically vibrated tool.

condition is approximated to be linear variation in the simulation model. Even though the force between the tool and the abrasive particle may alter the tool motion, it is assumed that the velocity variation keeps linear in the whole calculation. The tool velocity condition was applied to nodes on the top surface of the tool, and the calculation starts with the velocity value of 0.75 m/s. All nodes on the bottom and side surfaces of the workpiece were constrained in the direction of z and x/y axes, respectively. Before calculation, the tool tip surface and the work surface are completely flat. As the tool starts to touch the abrasive and forces the abrasive to penetrate into the workpiece, all parts begin to deform or fracture. The contacts between the abrasive and the tool and the abrasive and the workpiece were assumed frictionless. Effect of the liquid in slurry and its flow on the material removal is negligible, which means that only the abrasive particle was considered.

3.1.4. Simulation results

The time-dependent simulation results along X-Z symmetric plane are shown in **Figure 8**. The colors shown in the figure represent the state of the material. The green, blue, and red

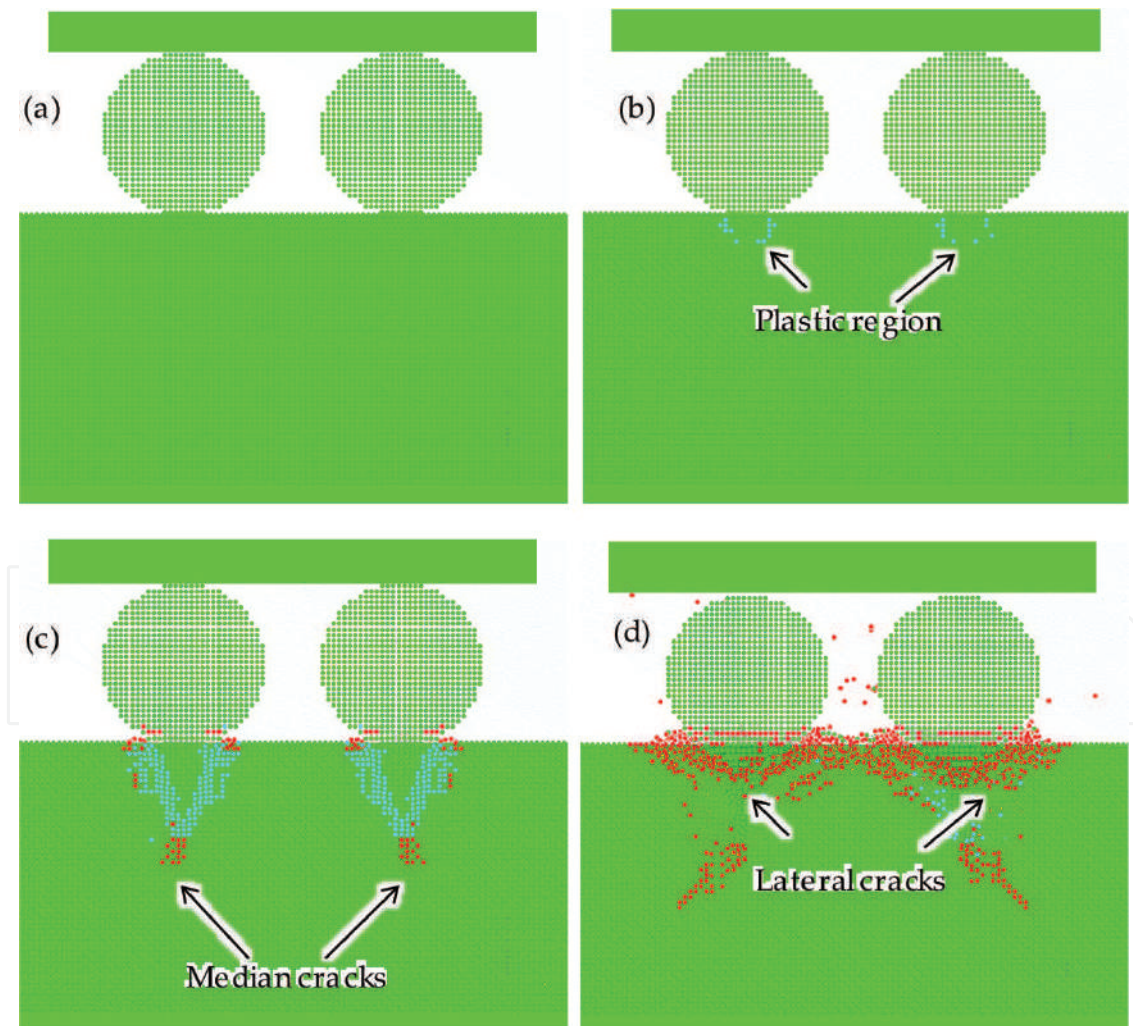


Figure 8. Simulation results of hammering actions by two adjacent abrasive particles: (a) initial condition, (b) after 0.1 μ s, (c) after 0.25 μ s, and (d) after unloading.

elements indicate elastic, plastic, and failure states, respectively. After $0.1 \mu\text{s}$ calculation, plastic zone induced by each of the two abrasive particles can be confirmed from the workpiece beneath the hammering location as shown in **Figure 8(b)**, which is the same as the result obtained from the single hammering calculation. With increase of the penetration of the tool, the median cracks initiate and propagate as shown in **Figure 8(c)**. A simultaneous fracture of the abrasives is also observed. With further penetration imposed by the tool, the cracks indicated in **Figure 8(c)** propagated into the surrounding material at an angle to the load axis instead of propagating parallel to the loading axis beneath the impact surface. In addition, the crushing of work material near the hammering site that is caused by each of the two abrasive particles became larger and larger as the loading displacement increases and finally coalesced. **Figure 8(d)** shows the final results after unloading. The lateral cracks also developed and propagated nearly parallel to the work surface after unloading.

3.1.5. Effect of the distance between impacts

Calculations were conducted by varying the distance between abrasive particles, and the results are shown in **Figure 9**. When the distance is within a specific range, the cracks are coalesced in the region between the impacts. With the increase of the distance between the two particles, the crack distribution becomes more similar to the one developed by a single impact, which means the interaction of the adjacent abrasive on the stresses in the region between two particles is decreased. The change of the material removal rate of the workpiece versus the distance between two adjacent abrasive particles is depicted in **Figure 10**. The material removal rate was defined as the mean volume of the materials removed by the mass of the two particles. It is noted that the interference between the two abrasive particles decreases when the distance between the two adjacent abrasive particles increases, which

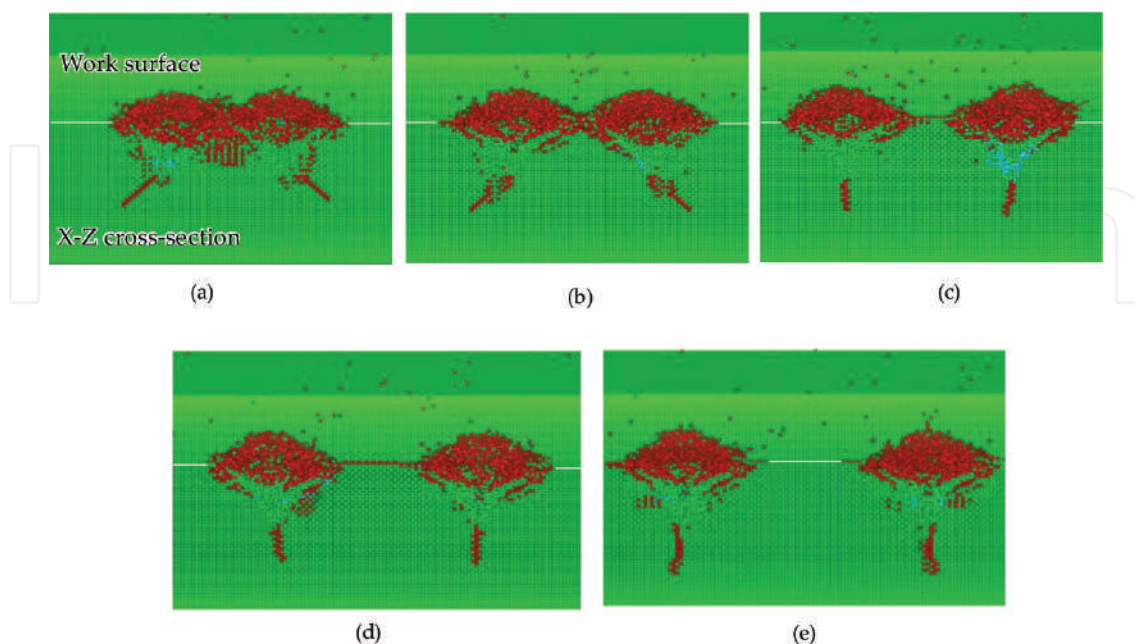


Figure 9. Effect of the distance between impacts: (a) $6.5 \mu\text{m}$, (b) $8 \mu\text{m}$, (c) $10 \mu\text{m}$, (d) $12 \mu\text{m}$, and (e) $14 \mu\text{m}$.

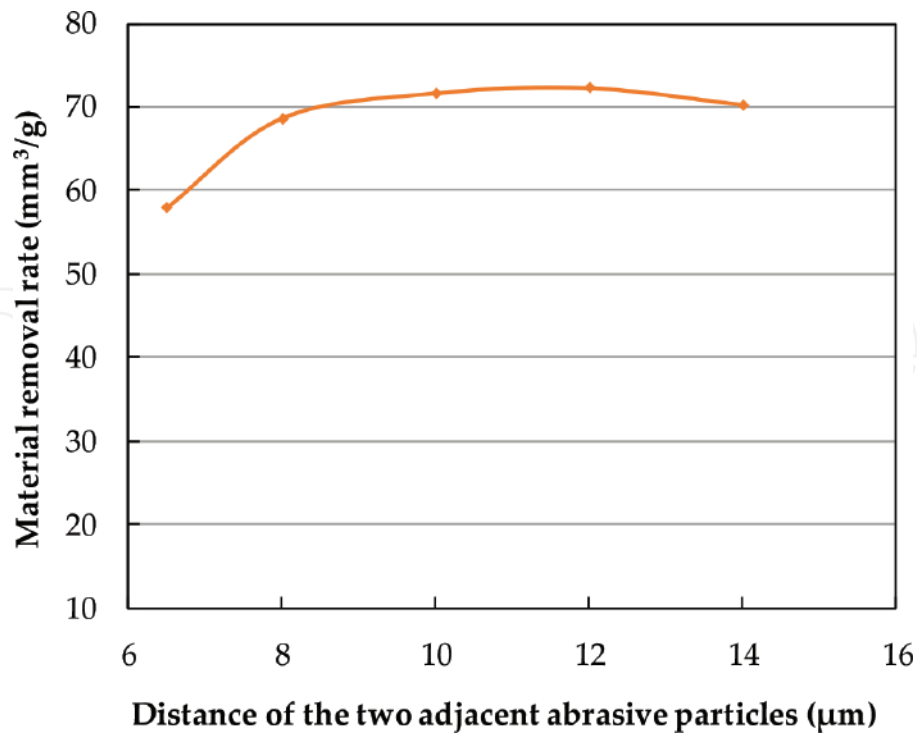


Figure 10. Effect of the distance between impacts on material removal of the workpiece.

increases the material removal rate. However, when a certain distance is exceeded, the interaction effect of the two adjacent abrasive particles is lost and the material removal would not be increased any more. The optimal distance for enhancing material removal rate was found to be 12 µm, twice the particle diameter.

3.2. USM experiments for verifying the simulation results

3.2.1. Experimental methods

USM experiments were conducted with different slurry concentrations for investigating the effect of the distance change among the abrasive particles. **Table 3** lists the experimental conditions. The machining was carried out with no circulation of slurry, and no tool feed was applied on the tool. A noncontact laser probe profilometer (Model: NH-3SP; Mitaka Kohki Co. Ltd., Japan) was used to scan across the machined area, and the volume of material removal was obtained by analyzing the three-dimensional surface topography. The cross sections of the machined surfaces were then created and examined using a scanning electron microscope (Model: SUI510; Hitachi Co. Ltd., Japan).

3.2.2. Experimental results

Figure 11 shows a schematic diagram of the experiment. In the simulation, only two particles were considered. However, there are a large number of abrasive particles worked on the workpiece in practical USM. Therefore, in order to verify the simulation results, the two parameters, i.e., material removal rate and distance of the two adjacent abrasive particles,

Vibration frequency (kHz)	61
Vibration amplitude (μm)	4 (peak to peak)
Tool material	SS304
Workpiece material	Glass
Abrasive (mesh size)	SiC #2000 (mean size, $8.4 \mu\text{m}$)
Concentration of abrasive slurry	5, 10, 20, 30, 40, and 50 wt% mixed with water
Distance between workpiece and tool (μm)	10
Machining time (s)	30

Table 3. Experimental conditions.

were defined for comparison. The material removal rate was calculated as the volume of the materials removed from the workpiece divided by the mass of abrasive particles in the machining zone as shown in **Figure 11**. The distance between two adjacent abrasive particles in the slurry was calculated from the slurry concentration according to a formula taken from previous work [29]:

$$C = \frac{(\pi/6) d_0^3 \eta \rho_g}{\lambda^2 d_0^3 \rho_g + (\pi/6) d_0^3 \eta (\rho_g - \rho_e)} \times 100. \quad (1)$$

in which abrasive particles with the same diameter d_0 are supposed to be equally distributed in the machining area and schematically shown in **Figure 12**. λd_0 is the distance between the two adjacent abrasive particles, C is the slurry concentration, η is the volumetric efficiency of the abrasive particle, ρ_g is the density of the abrasive material, and ρ_e is the density of the slurry medium. In this work, the abrasive particle is SiC and the slurry medium is water; the corresponding densities are $\rho_g = 3.2 \text{ g/cm}^3$ and $\rho_e = 1 \text{ g/cm}^3$, respectively. Parameter $\eta = 90\%$, which

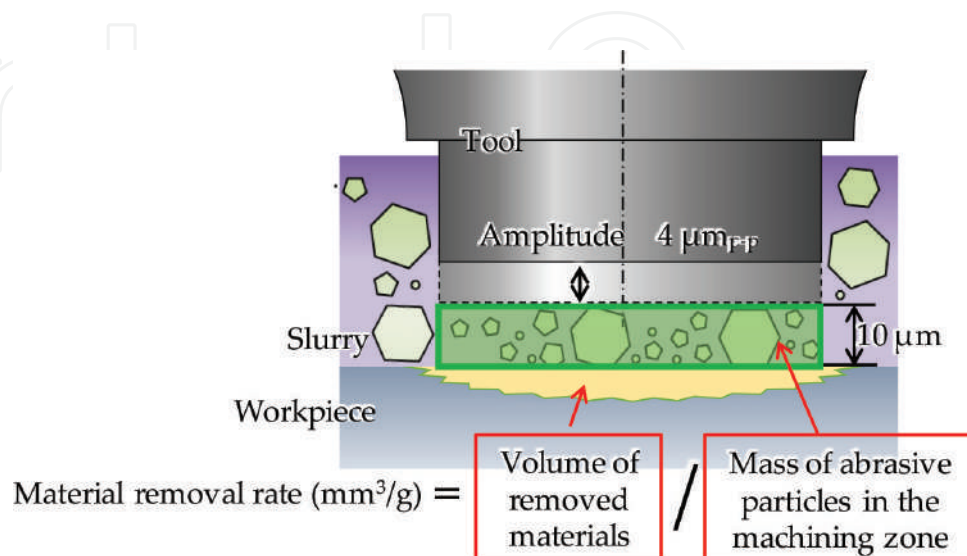


Figure 11. Schematic diagram of the experiment.

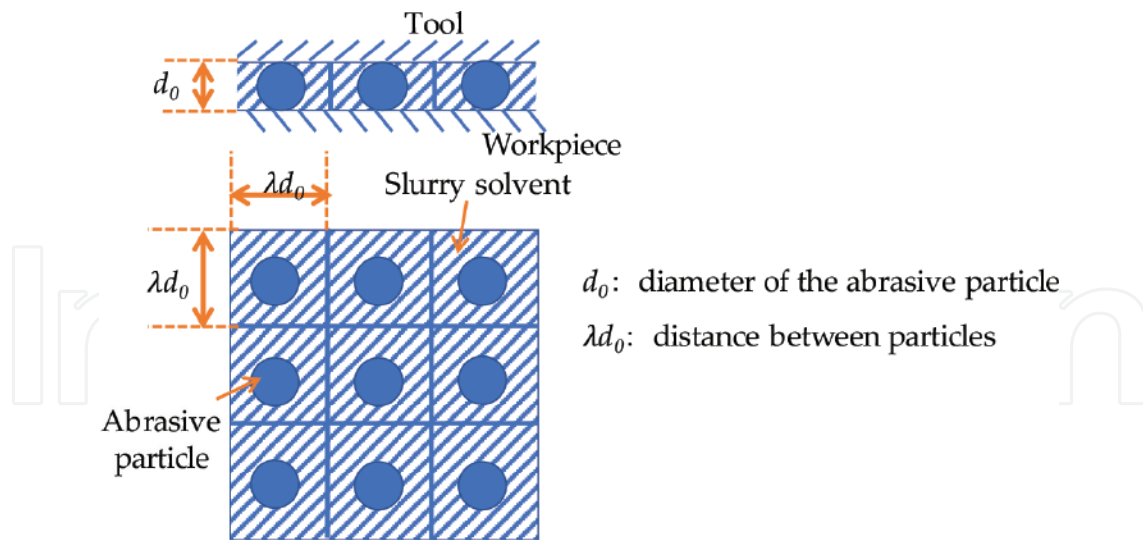


Figure 12. Distribution of abrasive particles in the machining area.

was determined by analyzing the abrasive particle shape using a particle analyzer (Model: Sysmex FPIA-3000; Malvern Instruments Ltd.). By substituting these values, λ under different slurry concentrations can be obtained. The relationship between the material removal rate and λ was determined and compared with the simulation results as shown in Figure 13. The simulation results were obtained from Figure 10, where the description of X axis was changed to λ by dividing the particle diameter $6 \mu\text{m}$ used in the model. The values obtained from

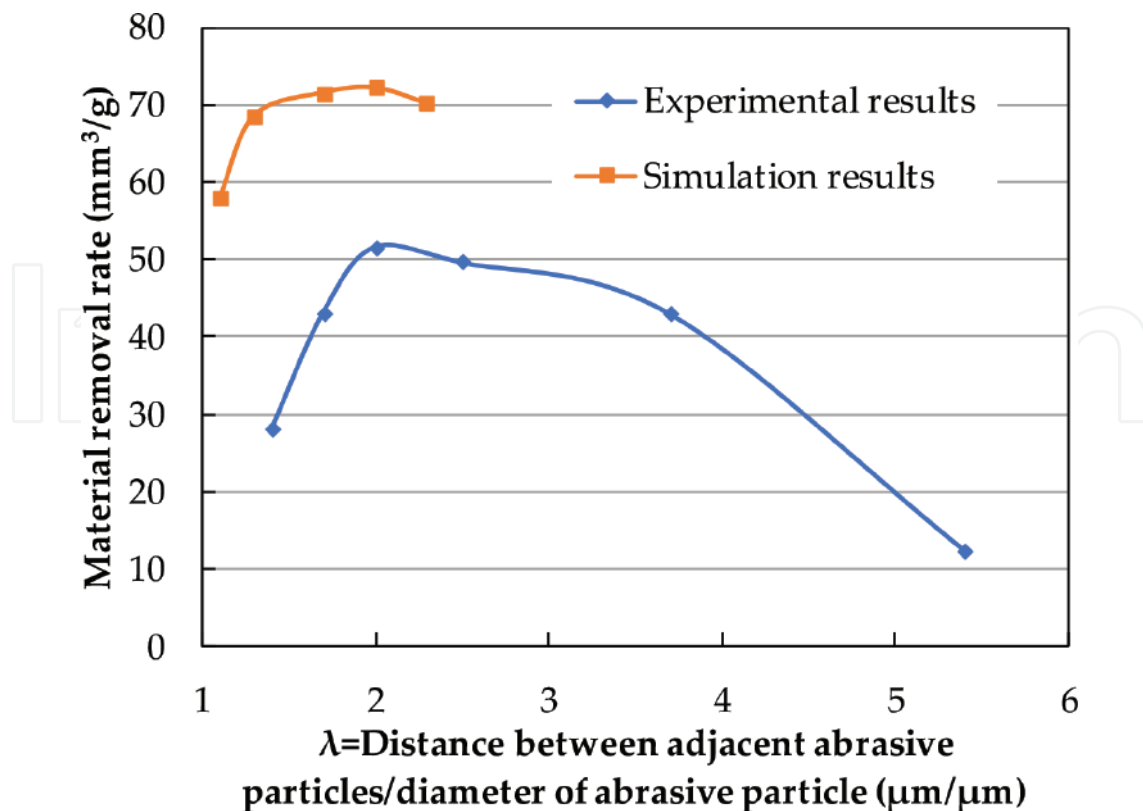


Figure 13. Effect of the distance between two adjacent abrasive particles on material removal rate.

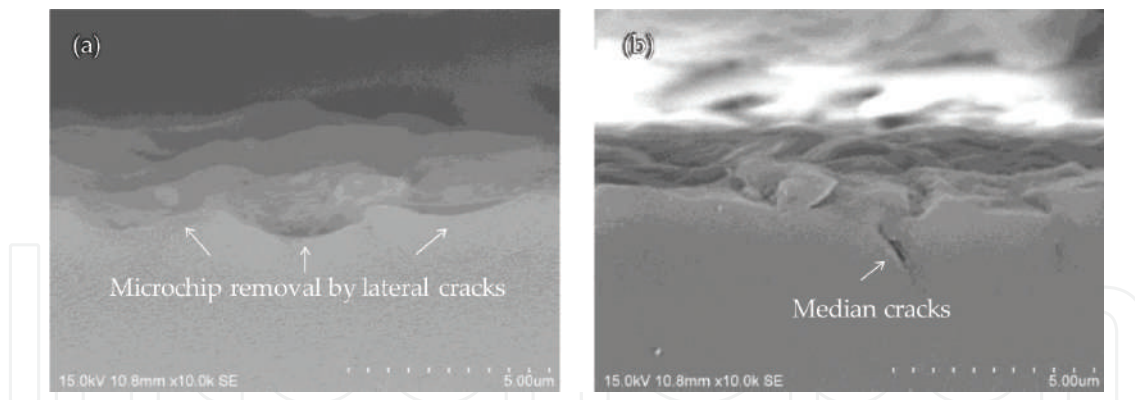


Figure 14. Cross sections of the machined surfaces: (a) microchip removal by lateral cracks, (b) example of median cracks.

the simulation results are constantly higher than those of experiments due to several factors including the nonuniformity of the abrasive particles in real machining process. However, both curves indicate that low material removal rate was obtained when the two adjacent abrasive particles are either very close or extremely far away. Maximum material removal was developed only when the distance between the impacting abrasive particles is optimal, which is found to be equal twice the diameter of abrasive particle from these results.

Although the material removal rate is influenced by slurry concentrations, the machined surfaces showed the same topography because materials are removed by the accumulation of cracks. **Figure 14** presents the SEM micrographs of cross sections of the surface machined by USM. From the micrographs, material removal via microchips which were occurred by the accumulation of lateral cracks can be confirmed. In **Figure 11(b)**, the median cracks remaining in the workpiece can also be observed. Both of the simulation and experimental results indicate that the material removal during USM is mainly caused by the accumulation of lateral cracks, while the median crack may play a less role. In addition, the median cracks that remain in the workpiece may cause subsurface defects and accordingly lower the quality of machined surface.

4. Summary and prospect

The current work introduced the background of the USM firstly. The importance of developing efficient micromachining technology for hard and brittle materials was stated. By comparing several machining processes, the potentiality of USM in micromachining of various hard and brittle materials was pointed out. Then, smoothed particle hydrodynamics method was proposed to study the material removal in USM and to reveal the influence of distance between two adjacent abrasive particles. The model was proven capable of simulating the crack generation in USM and helpful for predicting the machining results.

As the machining requirements of modern electrical, optical, and automotive components are getting stricter, there still exist many problems to be solved in the future for putting USM into practical industry. In micro-USM, the volume of material removed per stroke is very little due to the use of micrometer size abrasive particles. In fact, the corresponding machining speed is slowed down in order to obtain high form accuracy and superior surface finish

without large damages. However, with respect to a brittle material, microcracks are expected to be generated during this process and accordingly left on the machined surface. It is therefore important to find ways to remove these surface/subsurface cracks with no sacrifice of the machining speed, which means that the best balance machining conditions should be explored. A deep understanding of the mechanism and the effect of each machining parameter on USM needs to be given in future works.

Acknowledgements

The author gratefully acknowledges the support from Professor Tsunemoto Kuriyagawa, Associate Professor Masayoshi Mizutani, and Assistant Professor Keita Shimada at Tohoku University in Japan for their kind suggestions of my research work. The author would also like to thank Taga Electric Corporation in Japan with respect to the manufacture of USM tool and SmartDIYs Corporation for the provision of laser cutter parts for crack repair in the experiments.

The author would like to thank the financial support of “the Fundamental Research Funds for the Central Universities,” China [Grant no. 3132018259].

Conflict of interest

The author(s) declared no potential conflicts of interest with respect to the research, authorship, and/or publication of this article.

Author details

Jingsi Wang

Address all correspondence to: jixiewangjingsi@hotmail.com

Marine Engineering College, Dalian Maritime University, Dalian, China

References

- [1] Brow RK, Schmitt ML. A survey of energy and environmental applications of glass. *Journal of the European Ceramic Society*. 2009;**29**(7):1193-1201. DOI: 10.1016/j.jeurceramsoc.2008.08.011
- [2] Tsuboi R, Kakinuma Y, Aoyama T, Ogawa H, Hamada S. Ultrasonic vibration and cavitation-aided micromachining of hard and brittle materials. *Procedia CIRP*. 2012;**1**:342-346. DOI: 10.1016/j.procir.2012.04.061

- [3] Markov AI, Neppiras EA. *Ultrasonic Machining of Intractable Materials*. Iliffe: Scripta Technica, Inc.; 1966
- [4] Klocke F, Dambon O, Capudi Filho GG. Influence of the polishing process on the near-surface zone of hardened and unhardened steel. *Wear*. 2005;**258**:1794-1803. DOI: 10.1016/j.wear.2004.12.015
- [5] Komaraiah M, Reddy PN. A study on the influence of workpiece properties in ultrasonic machining. *International Journal of Machine Tools and Manufacture*. 1993;**33**(3):495-505. DOI: 10.1016/0890-6955(93)90055-Y
- [6] Egashira K, Masuzawa T. Microultrasonic machining by the application of workpiece vibration. *CIRP Annals – Manufacturing Technology*. 1999;**48**(1):131-134. DOI: 10.1016/S0007-8506(07)63148-5
- [7] Baek DK, Ko TJ, Yang SH. Enhancement of surface quality in ultrasonic machining of glass using a sacrificing coating. *Journal of Materials Processing Technology*. 2013;**213**(4):553-559. DOI: 10.1016/j.jmatprotec.2012.11.005
- [8] Tateishi T, Yoshihara N, Kuriyagawa T. Fabrication of high-aspect ratio micro holes on hard brittle materials—Study on electrorheological fluid-assisted micro ultrasonic machining. In: *The 4th International Conference on Leading Edge Manufacturing in 21st Century (LEM21)*; 2007
- [9] Thoe TB, Aspinwall DK, Wise MLH. Review on ultrasonic machining. *International Journal of Machine Tools and Manufacture*. 1998;**38**(4):239-255. DOI: 10.1016/S0890-6955(97)00036-9
- [10] Ghabrial SR. Trends towards improving surfaces produced by modern processes. *Wear*. 1986;**109**(1):113-118. DOI: 10.1016/0043-1648(86)90256-5
- [11] Sun X, Masuzawa T, Fujino M. Micro ultrasonic machining and its applications in MEMS. *Sensors and Actuators A: Physical*. 1996;**57**:159-164. DOI: 10.1016/S0924-4247(97)80107-0
- [12] Ichida Y, Sato R, Morimoto Y, Kobayashi K. Material removal mechanisms in non-contact ultrasonic abrasive machining. *Wear*. 2005;**258**(1):107-114. DOI: 10.1016/j.wear.2004.05.016
- [13] Kumar J, Khamba JS. Modeling the material removal rate in ultrasonic machining of titanium using dimensional analysis. *The International Journal of Advanced Manufacturing Technology*. 2010;**48**:103-119. DOI: 10.1007/s00170-009-2287-1
- [14] Zarepour H, Yeo SH. Predictive modeling of material removal modes in micro ultrasonic machining. *International Journal of Machine Tools and Manufacture*. 2012;**62**:13-23. DOI: 10.1016/j.ijmactools.2012.06.005
- [15] Singh R, Khamba JS. Taguchi technique for modeling material removal rate in ultrasonic machining of titanium. *Materials Science and Engineering A*. 2007;**460**:365-369. DOI: 10.1016/j.msea.2007.01.093

- [16] Agarwal S. On the mechanism and mechanics of material removal in ultrasonic machining. *International Journal of Machine Tools and Manufacture*. 2015;**96**:1-14. DOI: 10.1016/j.ijmachtools.2015.05.006
- [17] Kainth GS, Nandy A, Singh K. On the mechanics of material removal in ultrasonic machining. *International Journal of Machine Tool Design and Research*. 1979;**19**(1):33-41. DOI: 10.1016/0020-7357(79)90019-2
- [18] Lee TC, Chan CW. Mechanism of the ultrasonic machining of ceramic composites. *Journal of Materials Processing Technology*. 1997;**71**(2):195-201. DOI: 10.1016/S0924-0136(97)00068-X
- [19] Katahira T, Shimada K, Zhou T, Yan J, Kuriyagawa T. Material removal mechanism of ultrasonic machining. *Journal of the Japan Society for Abrasive Technology*. 2012;**56**(2): 108-111. DOI: 10.11420/jsat.56.108
- [20] Yu Z, Hu X, Rajurkar KP. Influence of debris accumulation on material removal and surface roughness in micro ultrasonic machining of silicon. *CIRP Annals—Manufacturing Technology*. 2006;**55**(1):201-204. DOI: 10.1016/S0007-8506(07)60398-9
- [21] Guzzo PL, Shinohara AH, Raslan AA. A comparative study on ultrasonic machining of hard and brittle materials. *Journal of the Brazilian Society of Mechanical Sciences and Engineering*. 2004;**26**(1):56-61. DOI: 10.1590/S1678-58782004000100010
- [22] Komaraiah M, Reddy PN. Relative performance of tool materials in ultrasonic machining. *Wear*. 1993;**161**:1-10. DOI: 10.1016/0043-1648(93)90446-S
- [23] Hocheng H, Kuo KL, Lin JT. Machinability of zirconia ceramics in ultrasonic drilling. *Materials and Manufacturing Processes*. 1999;**14**(5):713-724. DOI: 10.1080/10426919908914864
- [24] Johnson GR, Holmquist J. A computational constitutive model for brittle materials subjected to large strains, high strain rates and high pressures. In: *Shock-Wave and High-Strain-Rate Phenomena in Materials*. New York: Marcel Dekker; 1992. pp. 1075-1081
- [25] Johnson GR, Holmquist TJ. An improved computational constitutive model for brittle materials. *High-Pressure Science and Technology*. 1994:981-984
- [26] Holmquist TJ, Johnson GR, Grady DE, Lopatin CM, Hertel Jr ES. High strain rate properties and constitutive modeling of glass. In: *Proceeding of the 15th International Symposium on Ballistics*; 1995. p. 237
- [27] Holmquist TJ, Johnson GR. Response of silicon carbide to high velocity impact. *Journal of Applied Physics, Livermore*. 2002;**91**(9):5858-5866. DOI: 10.1063/1.1468903
- [28] Steinberg DJ. *Equation of State and Strength Properties of Selected Materials*. Livermore: Lawrence Livermore National Laboratories; 1996
- [29] Sato K, Matsui M. *Seimitsu Shiagehou (Precision Finishing)*. Kyoritsu Shuppan, Tokyo; 1958 (in Japanese)